Western&Graduate&PostdoctoralStudies

Electronic Thesis and Dissertation Repository

9-28-2020 2:00 PM

Development of an Optical Guide for Parabolic Dish Solar Collectors

Zane Charran, *The University of Western Ontario*

Supervisor: Siddiqui, Kamran, *The University of Western Ontario*
Joint Supervisor: Straatman, Anthony, *The University of Western Ontario*
A thesis submitted in partial fulfillment of the requirements for the Master of Engineering
Science degree in Mechanical and Materials Engineering
© Zane Charran 2020

Follow this and additional works at: https://ir.lib.uwo.ca/etd

⚙ Part of the Energy Systems Commons

Abstract

With the possibility of a global energy crisis on the horizon, the need for renewable energy processes is more crucial than ever before. Solar energy, specifically solar concentrated collectors can provide a green alternative to fossil fuel consumption, but several factors need to be considered to improve their efficiency and make them viable. The present research is aimed at the development of a novel "Optical Guide" to improve performance of traditional thermal receivers in Parabolic Dish Solar Collectors for use in a domestic solar water heater with PCM latent heat storage integration. Two ray trace programs, SolTrace$^{\text{TM}}$ and Tracer$^{\text{TM}}$ were used to model heat flux distributions developed at the bottom of the optical guide for various altitude angles with results indicating SolTrace$^{\text{TM}}$ to be the most accurate modelling tool for high resolution, reliable flux profiles. Generated flux distributions can be used to model heating mechanisms in the thermal storage unit, once favourable profiles for selected PCMs are determined. Mathematical modelling of the heat exchanger with integrated PCM, conducted under several assumptions to simplify heat transfer mechanisms, will be used to provide the framework for detailed development of the thermal storage system.

Summary for Lay Audience

Decreasing fossil fuel supplies for a potential uprising of global energy demand is a strong driving force to the development of efficient, renewable energy production. Solar concentrated collectors, unlike traditional PV solar cells, are capable of utilizing every wavelength of solar irradiance, allowing for extremely high performance efficiencies for these technologies. A deterrent in the feasibility of concentrated solar collectors is the losses associated when transferring heat collected to usable energy. The research proposes a parabolic dish collector system for use in domestic water heating utilizing a novel concept of reflecting all solar radiation to a thermal storage unit, the 'Optical Guide'. The novel optical guide will use optical physics for determination of component locations and will theoretically be able to transfer heat at higher efficiencies than traditional methodologies. Ray trace programs are used to model the flux that is produced in the optical guide to better understand heating mechanisms that occur in the thermal storage unit. Framework for a highly detailed mathematical model is developed and analyzed through alteration of key operating conditions for the solar water heating system.

Acknowledgements

Contents

List of Figures

List of Tables

List of Appendices

Nomenclature

Abbreviations

PCM - Phase Change Material
HTF - Heat Transfer Fluid
CSC - Concentrated Solar Collector
TES - Thermal Energy Storage
BRDF - Bidirectional Reflectance Distribution Function
NREL - National Renewable Energy Laboratory

Mathematical Symbols

y - Parabolic dish height [m]
a - Parabolic dish focal point [m]
f - Overall system focus [m]
f_1 - Primary dish focus [m]
f_2 - Seconary dish focus [m]
s - Gregorian-secondary spacing [m]
d_o - Distance between primary and secondary parabolic dish collector focal point [m]
d_i - Distance from mirror to concentrated rays [m]
θ_1 - Angle of Incidence [°]
θ_2 - Angle of Reflection [°]
ρ - Power of radiative reflectance [Dimensionless]
τ - Power of radiative transmittance [Dimensionless]
α - Power of radiative absorptivity [Dimensionless]
$e_b(T)$ - Total blackbody hemispherical emissiev power [W/m^2]
Λ - Radiative wavelength spectrum [m]
σ - Stefan-Boltzman constant [$W/m^2 K^4$]
T_A - Temperature of absorptive surface A [K]
ϵ_A - Emissivity of absorptive surface A [Dimensionless]
A_1 - Emitter surface [Dimensionless]
A_2 - Absorptive surface [Dimensionless]
$d^3 Pa(\tau, T_A, \theta i, \varphi_i)$ - Fraction of incident power absorbed at wavelength domain and direction [$W sr^{-1} m^{-2} Hz^{-1}$]
$i_{\lambda,i}(\lambda, \theta_i, \varphi_i)$ - Intensity of incident radiation at wavelength domain and direction [$W sr^{-1} m^{-2} Hz^{-1}$]
E - Energy absorbed [W]
F - Incoming flux [W/m^2]
A - Surface Area [m^2]
Q_{sc} - Solar collector heat transfer rate [W]

I_{sc} - Incident solar radiation [W/m^2]

η_{sc} - Solar collector efficiency [Dimensionless]

Q_w - Required energy for hot water load [W]

m_w - Mass of water for required load [kg]

$C_{p,w}$ - Specific heat capacity of water [kJ/kgK]

$T_{o,w}$ - Outlet temperature water [K]

$T_{i,w}$ - Inlet temperature water [K]

Q_{pcm} - Total thermal energy stored by PCM [kJ]

$C_{p,s}$ - Specific heat capacity of solid PCM [kJ/kgK]

$T_{i,s}$ - Temperature of initial PCM solid state [K]

T_m - PCM melting temperature [K]

L_f - Latent heat of fusion for PCM [kJ/kg]

$C_{p,l}$ - Specific heat capacity of liquid PCM [kJ/kgK]

$T_{f,l}$ - Final liquid temperature of PCM [K]

V_{PCM} - PCM voume [m^3]

m_{PCM} - PCM mass [kg]

$\rho_{PCM,l}$ - Liquid density of PCM [kg/m^3]

Nu - Nusselt number [Dimensionless]

h_i - Inner convective heat transfer coefficient [W/m^2K]

D_h - Hydraulic diameter [m]

k_w - Thermal conductivity of water [W/mK]

U - Overall heat transfer coefficient [W/m^2K]

r_o - Tube outer radius [m]

r_i - Tube inner radius [m]

k - Tube thermal conductivity [W/mK]

h_o - Outer convective heat transfer coefficient [W/m^2K]

$\dot{Q}_w$ - Heat transfer rate for hot water load [W]

$\dot{m}_w$ - Mass flow rate of water for required load [kg/s]

R_{tot} - Total thermal resistance [K/W]

A_{hx} - Required heat exchanger surface area [m^2]

Chapter 1

Introduction

Fossil fuels are the current primary energy sources worldwide, which include oil, natural gas and coal. As of 2011, 82% of the worlds energy demand was met by fossil fuels; with the United States generating 81% of their national energy supply by these sources [1, 2]. International Energy Agency has predicted that the reliance on fossil fuels will continue and by 2040, two-thirds of the global energy demand is expected to be met by fossil fuels [3]. Traditional energy production heavily relies on fossil fuels, yet they are a limited resource and can tremendously harm the environment. In high to middle income countries, 85% of airborne particle pollution and nearly all of the total sulfur dioxide and nitrogen oxide emissions to the atmosphere are generated as a result of energy related fossil fuel combustion [4]. Fossil fuel consumption accounts for a large portion of the human contribution to green house gasses; emissions that can potentially cause catastrophic effects to Earth's climate. About 35 billion tonnes of carbon dioxide emissions are injected into the atmosphere by humans every year as a result of energy use from fossil resources [5].

Domestic water and space heating are the predominant fractions of the total energy usage in North America. They account for nearly two thirds of total residential energy consumption in the USA [6] and about 80% by the Canadian residential sector [7]. Greenhouse gas emissions associated with domestic water heating in Canada increased over 10% from 1990 to 2002 and was responsible for 22% of Canada's total residential greenhouse gas emissions that year [8]. Air pollutants that result from greenhouse gas emissions are extremely harmful to urban areas and can have detrimental effects on the health of citizens. This danger is not only prominent only in high income countries such as Canada, but present across the globe as the World Health Organization claims only one in 10 persons live in a city that complies with their air quality guidelines [9]. On a global scale, the Annual Greenhouse Gas Index increased 40% from 1990 to 2016 and can be attributed to ever increasing CO_2 emission levels [10].

Current methods being developed to reduce the rate of greenhouse gas emission produced by fossil fuels, such as nuclear energy production and carbon capture and storage, could prove to be method of carbon reduction for electrical power generation. But with the world demand of renewable energy expecting to triple from 2008 to 2035, focus must shift to a safer, pragmatic solution for energy production [11]. Solar renewable energy systems can be easily implemented into residential environments and provide an attractive alternative to traditional electricity production; reducing the carbon footprint associated with residential heating. Solar concentrated collectors produce energy using the entire wavelength of insolation, collecting

all incident radiation and converting it into heat energy. The use of these collectors can prove to yield highly favourable results for domestic space and water heating, but require further advancements in their design to be suitable for such application. A major contributor to thermal losses in solar collectors is the process of transforming solar radiation into usable energy. This process involving convective losses between heat transfer fluid and the collector system along with re-radiative losses due to the extremely high temperatures developed at the receiver surface, leads to approximately 20%- 40% of energy being lost in a parabolic dish collector's thermal receiver [12].

Parabolic solar collector systems are relatively more expensive than conventional non-concentrating solar thermal collectors, making these technologies not feasible for many applications. An impact of this magnitude to system performance greatly reduces the feasibility of solar water heaters for domestically scaled applications, thus the need for more efficient methods of energy collection and transference must be developed before residential usage integration. Efficient methods of transforming solar radiation to usable thermal energy will allow concentrated solar collectors to have a higher contribution in renewable energy production; but current limitations must be addressed for this to be achieved. Current theory suggests that losses associated with re-radiation and convective heat transfer in parabolic dish solar collectors can be reduced through implementation of a receiver system that reflects incident solar rays to a fixed ground thermal interface.

1.1   Background

1.1.1   Concentrated Solar Collectors

Solar collectors are placed in three categories, low, medium and high temperature collectors [13]. Low temperature collectors operate at a range below 100°C and are typically used for small scale space heating; while medium and high temperature collectors, operate at 400°C and higher, can be used for water heating aswell as electrical power generation [14] Among solar energy collecting systems, concentrated solar collectors are considered to be more efficient than flat plate collectors. Concentrated solar collectors are typically parabolic in shape and reflect incident solar radiation onto a small absorbing surface located at the focal point, converting it into heat (see Fig. 1.1).

(a) Flat Plate Collector (Low
Temperature)

(b) Parabolic Dish Collector
(Medium to High
Temperature)

(c) Parabolic Trough Collector
(Medium to High
Temperature)
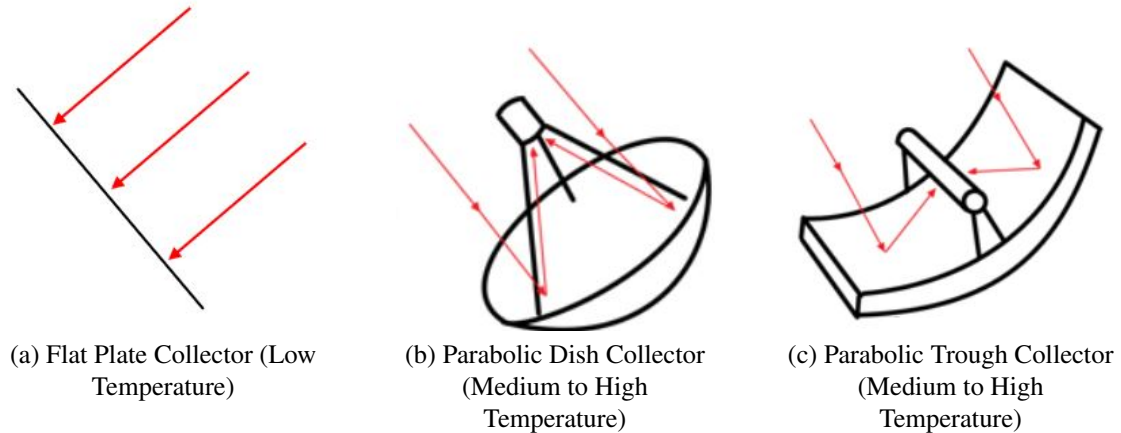
Figure 1.1: Types of solar collectors [15]

A Parabolic dish collector consists of a parabolic dish used to concentrate solar radiation onto
a focal point (see Figure 1.1b). A parabolic geometric profile redirects rays incoming parallel
to the dish's axis and be reflects them to the focal point, and due to the immense distance
between the sun and the earth, incident solar rays always strike the earth's surface at near
parallel incidence. It is because of this that a dual-axis tracking system is typically incorporated
to a parabolic dish solar collector. The tracking system is used to align the dish's axis to the
sun (azimuth and altitude angles), allowing for incoming rays to be parallel to the parabolic
dish [16]. Traditional parabolic dish solar collectors contain a thermal receiver at the focal
point capable of converting the concentrated solar energy into heat and if necessary, heat into
mechanical work, such as a Stirling engine. Losses associated with this system are usually
a result of imperfections in reflective materials used as well as energy losses at the receiver
(rereadiation losses and losses due to conversion efficiency) [17]. Concentrated solar collectors
have relatively high efficiencies for their low costs, thus vigorous research is currently taking
place to optimize their designs.

1.1.2 Solar Water Heaters

Traditional solar water heaters utilize a flat-plate solar collector designed for optimal solar
absorption. A large fraction of the solar radiation intersecting the highly absorptive collector
surface is transferred to a fluid circulating inside the collector for use in a heat exchanging
system that is directly, or indirectly connected to a domestic water tank (see Figure 1.2).
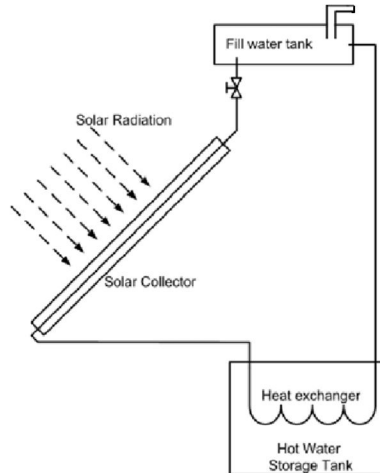
Figure 1.2: Solar water heating unit [18]

Solar water heaters can be classified as one of two systems, passive or active. Passive systems take advantage of circulation induced by natural convection to transfer heat a storage tank located above the solar collector, while water is passed through the collector by means of an electrical pump in active systems. Both configurations can be used to supply hot water for domestic usage at approximately 60°C, but passive systems are the most commonly used [19]. Active systems are superior in multi-floored buildings as the collector does not need to be close to the water storage tank but prove to have drawbacks in terms of electrical dependency and overall complexity. Due to the implication of an active pump, trained personnel are required for adequate operation of these systems, rendering overall operating costs higher than that of a typical passive system [20].

The method of transferring heat to the water storage tank is achieved one of two ways, directly and indirectly. Direct solar water heaters circulate water between the collector and water storage tank without usage of a heat exchanger, whereas indirect heaters employ a heat exchanger and carefully selected heat transfer fluid. A heat exchanger inside or outside of the water storage tank improves heat transfer from the collector to working domestic water. It is because of this that indirect water heating systems generally perform better than their counterpart [21]. Domestic water tanks are typically insulated and contain secondary electrical heaters for instances where solar loading is lower than anticipated.

1.1.3   Thermal Energy Storage

Solar thermal systems are limited by the exposure time and intensity of solar irradiation, rendering them obsolete during the time of low irradiation or at night. One of the most important factors of efficiency is the ability to retain collected energy for later usage. Thermal energy storage is the concept of accumulating thermal energy when available, in a storage system for later usage, primarily for domestic heating and industrial processes [22]. With this technology it is possible to store solar thermal energy collected by solar concentrators during the daytime for use at night, essentially yielding a usable period of operation larger than previously predicted. Thermal energy storage systems increase overall efficiency by retaining absorbed energy, lead-

ing to installation and operating cost reductions as well as lower greenhouse gas emissions [23]. Various types of thermal energy storage systems exist such as concrete media storage, molten salt heat transfer fluids, chemical storage and phase change materials [24, 25, 26].

Energy per unit mass, or energy storage density, is of utmost importance when optimizing efficiency and energy consumption of solar thermal energy systems. Thermal energy storage traditionally consisted of storing energy in the form of sensible heat by raising the temperature of water for later use but proved to be inefficient with limited storage capacities [27]. A more efficient method of energy storage involves the exploitation of latent heat (high storage capacity per unit mass) by using phase change materials (PCMs). Phase change materials used in thermal energy storage systems typically undergo solid-liquid phase transition and have a significantly higher latent heat of fusion than specific heat capacity, thus can store and release heat at a greater rate during phase change than that of a sensible heat energy storage system [28]. As presented by Jevnikar et al. [29] three main stages of heat transfer will occur within phase change materials during melting; strong conduction, strong natural convection and then a weakening natural convection. A strong conductive heat transfer is present when PCM is solid but vanishes when melting temperature is reached, then natural convection is the predominant mechanism. A weakening natural convective force is observed at later points during melting when stagnated liquid PCM regions inhibit heat transfer by reducing recirculation of material. They also concluded that heat source angle of orientation influences melting behaviour of PCM; with inclined variances producing less regions of stagnated liquid PCM, thus higher rates of heat transfer compared to vertical (0° tilt) heat sources.

A phase change material releases (discharge) or absorbs (charge) energy upon phase transition and can be used for useful thermal energy storage for several reasons. A main advantage is their ability to store energy in the form of latent heat, allowing for greater capacity of energy retention than that of a sensible heat storage system. As PCMs change phase, energy storage density increases; latent storage systems take advantage of this fact and thus have lesser volumes to that of their sensible storage system counterparts [30]. These materials must have high latent heat properties with a melting temperature within the desired operating range. PCMs provide advantages in thermal energy storage due to their high energy density and in turn manageable size as well as their isothermal latent storage process. As a result, a tank with a PCM is able to absorb significantly more heat than that of a tank with just water. A wide variety of materials are being studied as PCMS including paraffin waxes, eutectics of organic and inorganic compounds and fatty acids [31]. Storage capacity of PCMs can be increased based on material composition, with research from Bashar et al. [32] concluding that introduction of nanoparticles to PCM mixtures significantly increase performance. They found that the integration of copper nanoparticles to paraffin wax phase change material increased heat flux and melting rate by 25% compared to that of the plain PCM case, along with an increase of transient heat transfer coefficient by 18% .

1.1.4 Solar Radiation

Solar radiation is emitted at several wavelengths throughout the electromagnetic spectrum, but nearly 99% of solar radiative energy lies within the wavelength of 0.15μm to 4μm. Less than 1% of solar radiative energy lies within the wavelengths of gamma rays, x rays and radio

waves; while approximately 43% of energy is within the visible spectrum, 49% lies within the near infrared spectrum and 7% in ultraviolet [33]. Traditional solar photovoltaic cells utilize a material that typically uses only the visual light spectrum to generate electricity as only solar radiation within the wavelengths of 380nm to 750nm can create enough energy to generate an electrical current [34]. The remainder of energy absorbed in solar cells is converted to heat and wasted. However, concentrated solar collectors convert all solar radiation into heat, allowing a greater utilization of solar energy (see Figure 1.3).
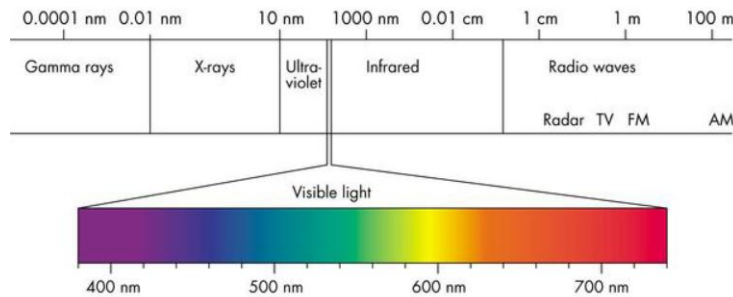
Figure 1.3: Electromagnetic spectrum [35]

A value known as the "Solar Constant" measures the amount of solar energy per unit time and area irradiated from the sun at an average distance away from the earth. The most accurate value recorded of the solar constant is $1,365W/m^2$ [36]. Radiation emitted from the sun is scattered and absorbed in earth's atmosphere. The distribution of energy proportional to circumsolar irradiation is known as the "Sun Shape" and is highly dependent on location and atmospheric conditions [37]. An accurate sun shape must be calculated in order to determine performance of solar collectors at a given location, since this heavily influences the radiative flux distribution developed in the solar focusing systems. A common method of applying sun shape profiles to solar radiative modelling involves use of solar ray tracing; computational programming that incorporates the Monte Carlo algorithm with classical geometric optics[38]. Ray tracing essentially uses the Monte Carlo probability model to set the direction, position and energy of rays to simulate their respective optical paths.

1.2   Literature Review

1.2.1   Parabolic Dish Collector

One of the earliest propositions of parabolic dish solar collector design was established in 1990 by Bomin-Solar by taking a segment of a paraboloid and rotating it around the focal point corresponding to the solar incident angle [39]. Based on a $2500kW/m^2year$ input and a 100MW electrical output, they determined the dish would yield an annual efficiency of 25% at a yearly maintenance cost of $25.8/$m^2$; while producing $62.5/$m^2$ worth of electricity per year. This technology was deemed economical for its 20 year life span.

A study conducted in 1985 by Panda et al. [40], for the U.S. Department of Energy analysed several parabolic dish collector configurations with operating temperatures from 315°C to over

1300°C. They described different receiver types for parabolic dish systems and their respective efficiencies. It was shown through their research that favourable performances could be achieved through application specific receiver design. Sanders and Garret's air Brayton and steam Rankine cycle receivers were found to be superior with overall efficiencies of 25% to 33% between a temperature range of 900°C and 1400°C. While these yielded more desirable results for large scale energy production, the experimental 'Solar-Only' receivers consisting of a Stirling engine returned similar efficiencies for temperatures between 300°C and 600°C (see Fig.1.4).

(a) Cross Sectional Air Brayton   (b) Cross Sectional Steam Rankine
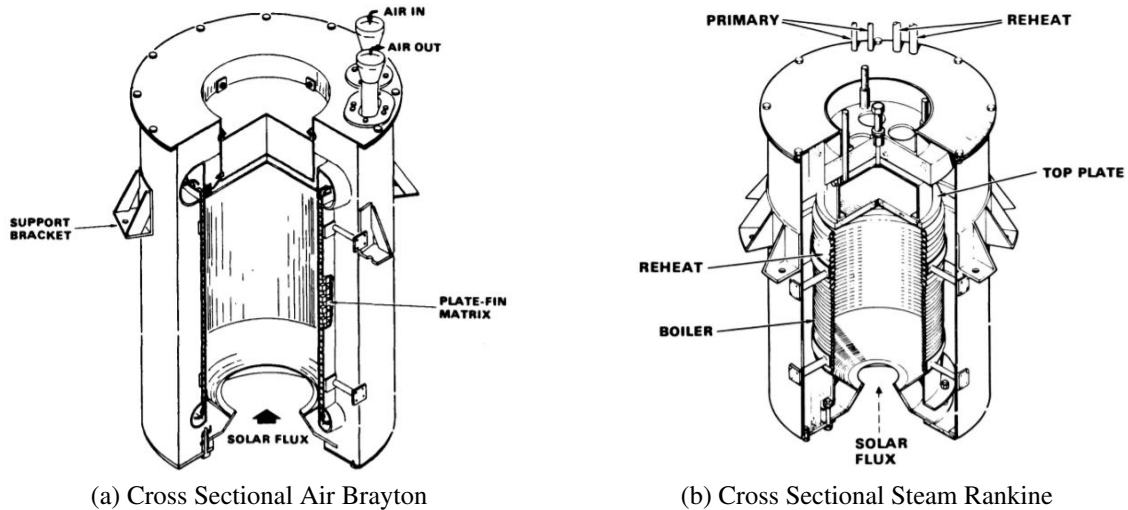
Figure 1.4: Garret air Brayton receiver and steam Rankine receiver schematics [40]

A method of storing thermal energy in a thermochemical receiver of a concentrated solar collector was proposed by Zheng et al. [41]. This study developed a methane reforming thermal receiver that when reacted with high temperature steam, produces highly endothermic reactions that can store solar energy in the form of chemical energy. These type of receivers are connected to heat exchangers and react when the circulated water generates enough heat from the solar collector. The study concluded a thermal loss independent of input temperature to be 2 kW, while overall efficiencies were found to be 69% when the receiver was connected to a 4.7m diameter, 12kW parabolic dish collector. A similar concept was presented in the study of Lovegrove et al. [42], where ammonia was used instead of methane. Advantages of ammonia include no possible side reactions, endothermic reaction operates within the range of solar collectors and requires an easily achievable handling pressure of about 30MPa. Their conclusions for the receiver on a $20m^2$, 15kW parabolic dish collector indicated that operating temperatures of 391°C would yield a thermal efficiency of 70%, an approximate 74% heat exchanger efficiency and an overall energy storage efficiency of 52%.

Solar Kinetics, Inc designed a 7m diameter dish using a plastically deformed pre-shaped front membrane, and polyester cloth resin for a back membrane [43]. This solar collector, built in 1991, incorporated the "Stretched-Membrane" design methodology of holding a membrane in tension on the outer surface of the primary reflector, increasing the stiffness. It was found that these concentrators offer a possibility of significant cost savings over traditional production

methods, but access to inexpensive, durable membrane material is limited. The Solar Kinetics, Inc design incorporated a traditional Stirling engine receiver with an approximate efficiency of 25%.

Ali et al. [44] conducted a performance analysis on the steam generating Invictus 53S parabolic solar collector, determining several of the systems efficiencies . The Invictus 53S is consists of a dual axis, azimuth-elevation tracking system mounted on a pedestal and a 9m diameter dish consisting of 15 mirrors. They concluded that the system was capable of maintaining superheated steam at an average temperature of 320°C with a thermal efficiency of about 93%; surpassing industry standards of 88% with traditional steam generators. Along with the exceptional thermal efficiencies, this solar collector proved to be optically superior to its parabolic trough and reflecting tower counterparts. A net optical efficiency was yielded at 95.4%, with 96.1% of solar radiation reflected from the dish to focal. High efficiencies were largely a result of dual axis tracking and large concentration ratios, a trait unique to parabolic dish collectors.

A detailed comparison of a concentrated solar plant to that of a photovoltaic plant was presented by Desideri et al.[45] describing the most cost effective solution for plants located in the south of Italy and Egypt. The findings of this study stated that for the same production load, the concentrated solar collectors displayed higher annual electricity production (40.7GWh) than that of a photovoltaic module (10.6GWh). Results also depicted that although concentrated solar collectors out perform their counterpart, photovoltaic plants yield a higher efficiency for land usage due to their reduced operating space. Results between Italy and Egypt remained consistent with concentrated solar facilities yielding to be the most economic option for electricity generation due to their ability to store thermal energy.

Comparison of the cost and sizing of solar thermal flat-plate collectors to building-integrated photovoltaic thermal cells are presented in a study by Gautam et al.[46], in which these two systems were configured for electricity production and water heating. They concluded that if electricity and heat have the same price, solar thermal collectors save more money than building-integrated photovoltaic thermal cells. Results showed that thermal solar applications outperform the building-integrated photovoltaic cells with an overall thermal efficiency of 58% for thermal only applications compared to 33% for the building-integrated photovoltaic cells. They also depicted 80% supply of demand with a collector area just of $250m^2$, whereas building-integrated photovoltaic cells were completely incapable of producing that solar fraction. Although solar only systems produce more usable energy; for locations where electricity is more expensive than heat, building-integrated photovoltaic cells are the most attractive option as photovoltaic cells produce 4.6% more electrical energy.

1.2.2   Phase Change Material

Phase change materials are a potential storage media in to thermal energy systems, but further research must be conducted to improve understanding of the fundamental heat transfer processes during phase change, which are vital to design high-efficiency thermal energy storage systems. A study by Naim et al. [47] examined the performance of a single stage solar still used for water desalination with a material mixture used for thermal energy storage. Results showed that the optimum phase change energy storage mixture was a specific ratio of paraffin wax, water, paraffin oil and aluminium to improve conductive heat transfer. The energy storage

mixture integrated into the single stage water still was determined to increase the productivity of distilled water with a limiting reagent of saline concentration in the water. While higher saline concentration in the supply water would lower productivity in the solar still, higher flow rate and temperature of saline supply water improved efficiencies. The integration of an energy storage system allowed greatly improved performance for overnight water distillation. Solar still efficiency, measured by the ratio of energy put into water distillation and the solar energy absorbed over an operating time, resulted to be 36.2%. An operating period including a 6h daytime period and nightly water distillation results indicated a maximum productivity of $4.536L/m$ at a saline flow rate of $40mL/min$.

The performance of a solar still with a paraffin wax latent heat storage system, designed for heating and humidification of a green house was analysed by Radhwan [48]. The experimental set-up consisted of an insulated bottom under five stepped basins and an inclined glass cover (see Fig.1.5). Paraffin wax acted as the phase change material and placed under the basin in order to perform as a latent energy storage medium. The greenhouse air would flow into the bottom of the apparatus and through the basins and glass cover, being heated and humidified before returning to the greenhouse. Results indicated that the configuration with a latent heat storage system had slightly less thermal efficiency and daily production yield than that without a storage system; mainly a result of the five hour melt time for the paraffin wax specimen. However an insignificant decrease in efficiency was heavily outweighed by the latent heat storage system's ability to heat and humidify the green house at night, a period of time most crucial to this application. Thermal efficiency was calculated based on the ratio of effective heat gained to the insolation and collector area for a period of time. The solar still with a latent heat energy storage system retained a total daily yield of $4.6L/m^2$ at an efficiency of 57% where as the system without a storage system produced $4.6L/m^2$ at 61% efficiency. Although the paraffin wax integration indicated lower daytime efficiencies, these systems are able to store heat for the following day's initial condition and within less than a week began to supply the greenhouse for the entire duration of consecutive days. Relative humidity conditions of air supplied to the greenhouse were also indicated to be consistently satisfied.
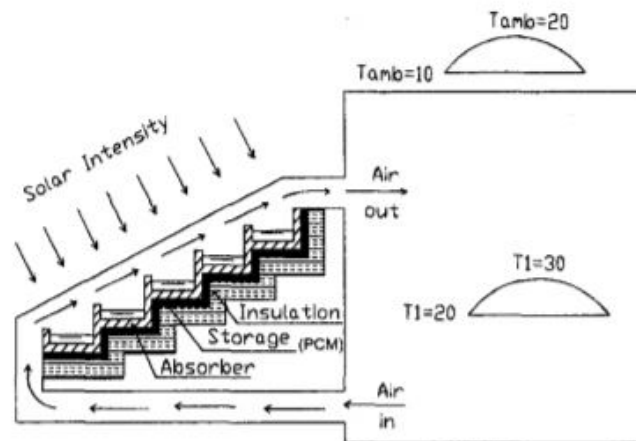
Figure 1.5: Glass enveloped solar still with paraffin wax latent heat storage schematic [48]

Mettawee et al. [49] experimentally investigated the performance of a phase change material

solar collector based on latent heat energy storage. This experimental setup consisted of a solar absorbing plate housing the paraffin wax phase change material which discharged heat into pipes carrying cold water as a heat transfer fluid. Outdoor experiments were conducted on a collector of $1m^2$ effective area used for water heating. They concluded that the useful heat gain of phase change material increases proportionally to the input mass flow rate of cold water. They observed that the overall average heat transfer coefficient was very small at the start of the melting process during charging;leading to the conclusion that the main mechanism of heat transfer is conduction. However over time, the rate of heat transfer increased; largely due to growth of natural convection currents in the melted layer of the material. Conclusions also indicated that due to the low conductivity of paraffin wax, useful heat gain decreases with time as the wax begins to solidify.

Thermal performance based on the heat transfer rate per unit area and the bulk fluid temperature gradient at the outlet of five heat exchanges, utilizing RT35 paraffin wax as a phase change material for heat transfer media in small residential applications are presented by Medrano et al. [26]. This study investigated the charging phase (melting) and discharging phase (solidification) of paraffin wax in different heat exchanger configurations and operating condition. Results indicated that faster phase change is achieved by higher heat transfer fluid velocity in the exchanger tube, indicating that the optimal operation occurs at higher Reynolds numbers, specifically in the turbulent flow regime. Water inlet temperature also played a crucial role in phase transition time as an increase of inlet temperature from 15°C to 25°C resulted in an increased rate of heat transfer to the material, thus a decrease in phase transition time from 30% to 60%. The study also indicated that double pipe and plate heat exchangers do not adequately store heat as a result of small heat transfer area or a low ratio of heat transfer capacities. A configuration of a compact heat exchanger with phase change material in-between the coil and adapted fins yielded the highest average heat transfer rate. Experiments were also conducted at lower temperature differences showing that the compact heat exchanger configuration performed three times better than the second best heat exchanger in terms of rate of heat transfer.

Results for outdoor experiments conducted on a flat plate solar collector with an integrated thermal storage unit are presented in a study by Al-Kayiem et al. [50]. Performance for water heating was determined for systems without thermal energy storage, with paraffin wax as a phase change material and with a nano-composite of paraffin wax and copper for solar collector inclination angles of 10°, 20° and 30°. The water heating system was evaluated in a 12 hour period starting at 7:00AM for a 60L storage tank. Optimal conditions proved to be at a 10° inclination angle with a water flow rate of 0.5 kg/min. After 24 hours of operation the systems integrating thermal storage, i.e., the paraffin wax and nano-composite paraffin wax and copper, maintained water temperatures of 40.1°C and 40.7°C respectively; while the system without a thermal energy storage only maintained a temperature of 35.1°C. Results indicated that the solar water heating system with the nano-composite of paraffin wax and copper yielded the highest efficiency of 52.0%, while the paraffin wax only phase change system has an efficiency of 51.1%. The system without thermal storage yielded an efficiency of 47.6%. This study highlights the use of phase change materials as an enhancement in thermal storage systems and the insignificant benefits of incorporating nano-composites.

The thermal performance of an integrated collector solar storage water heater was analysed by

Chaabane et al. [51]. Analysis consisted of a 3D computational fluid dynamics (CFD) model of the two phase change materials, myristic acid and RT42-graphite, at three different radii 0.2m, 0.25m and 0.3m of the tank. A sensible heat storage system was compared to the latent heat storage systems described above to determine the configuration with the most favourable performance during certain operating conditions. Results showed the benefit of using latent heat storage units during night operations regardless of phase change material used. This is heavily due to both phase change material systems possessing lower thermal losses and better heat retention. In terms of day-time operations, the latent heat unit only performs better than the sensible unit, but only with the use of myristic acid as the phase change material. Myristic acid as a phase change material provides maximum water temperatures 12°C higher than that of RT42-graphite due to higher energy release during the melting process, suggesting it was the more suitable phase change material for this solar application.

Variation of water temperatures in a passive solar water heating system integrated to salt hydrate phase change materials was experimentally investigated and compared to a traditional system without a phase change material storage unit by Aksoy et al. [52]. A flat plate solar collector 1.94m wide, 0.94m long was used to collect heat for residential water usage in an 80L storage tank. Operating conditions required the solar collector and phase change storage unit to provide water at 45°C from a feed water temperature of 15.5°C. Utilizing a 110L capacity tank with salt hydrate phase change material integrated for latent energy storage they determined that the monthly time-averaged water temperatures of the storage tank decreased steadily during each day until the melting temperature of the phase change material was reached. Once this temperature was obtained, stored water was able to maintain an average temperature of 45°C for approximately 10 hours until sunrise. The phase change material integrated water heater provided water at an outlet temperature 6°C higher than that of the system without a latent heat energy storage; providing confidence in the systems effectiveness. Results indicated a nearly 300% increase in the total heat generation, hot water production and storage time with the addition of salt hydrate phase change materials (disodium hydrogen phosphate dodecahydrate and sodium sulfate decahydrate). These results indicate that the use of phase change materials in these applications leads to lower costs associated with solar water heating as sizing requirements for insulation and thus heating tanks are decreased with retained thermal energy in an energy storage.

1.2.3   Solar Water Heating

Chuawittayawuth et al. [53] experimentally validated theoretical models of solar water heaters through observational analysis under clear, partly-cloudy and cloudy conditions. The solar collector used for experimental analysis consisted of an absorber plate integrated into a thermosyphon solar water heating system, taking advantage of natural circulation rather than using a pump. The collector heats feed water running through riser and header tubes, connected to the hot water storage tank. The results show that water and absorber plate temperatures were significantly higher during clear skies and poses insignificant changes between partly and fully cloudy conditions. Water experienced an average temperature rise of about 14°C to 17°C for partly cloudy conditions as incoming insolation is highly fluctuated. Expectedly, clear sky conditions yielded the highest water temperature rise of about 21°C to 24°C. Overall the exper-

imental values match theoretical models studied, with a maximum flow rate through connecting pipes of approximately $17cm^3/s$ to $22cm^3/s$.

Roonprasang et al. [54] developed a solar water heater using a solar water pump; powering itself with steam produced by a flat plate solar collector. They described the optimal thermal performance of their solar water heater being dependent on discharge head and incident solar radiation, with peak performances achieved at $580W/m^2$ and $630W/m^2$ for a discharge head of 1m and 2m respectively. These results indicated a non-linear relationship between daily water production and daily insolation; also depicting the same for thermal and daily pump efficiencies. Storage tank water temperatures ranged from 46°C to 61°C, an acceptable value for domestic hot water supply. Water circulation throughout the solar domestic water heater was in the range of 12L/day and 59L/day. Results indicated that water circulation is highly dependent on solar insolation, thermal energy losses within the system and discharge head.

Passive and active solar water heating systems were compared to each other in a study conducted by Khalifa [55] through experimentation of two flat plate solar collectors (one passive and one active) each with area equal to $1.42m^2$, tilted to an azimuth angle of 45° and feeding a 170L storage tank. It was determined that active systems produced efficiencies, based on the ratio of useful energy output to daily solar radiation, of 35% to 80% higher than that of passive systems essentially as a result of forced circulation. The aforementioned study agrees reasonably with the results of Lee et al. [56] depicting the differences in passive and active solar water heating systems for urban areas. Lee et al.[56] experimentally measured the thermal properties of passive and active solar water heaters integrated onto three flat plate collectors each of $6m^2$ aperture area. The solar collectors, inclined to an angle of 40° were used to partially supply heat to a hot water storage tank of 305L capacity using an active circulation system that activates when inlet and outlet temperatures differ by at least 6°C. Similar to results presented from Khalifa [55], the active system yielded a higher efficiency of 69% while the passive system produced a thermal efficiency of 61%. Results from this study also depicted active systems maintaining overall heat transfer coefficients twice as great to their counterparts and, for maximum efficiency of both solar water heater configurations, nightly water withdrawal should only occur once.

A cylindrical shaped solar water heater storage was designed and tested for residential use by Nahar et al. [57]. It consisted of a coiled copper tube housed in a glass pipe (to allow solar radiation to enter the tank). The copper coil was painted black and contains a heat transfer fluid, acting as the solar collector. Results indicated that the designed storage tank could supply 50L of hot water at 50°C to 60° in the afternoon; while the stored water was able to retain a temperature of 35°C overnight for a morning use. Their results indicated that cylindrical solar collectors are about 30% more productive than that of flat plate collectors when used for solar water heating.

Brown et al. [58] described a model used to estimate energy inputs required to predict the output energy of any given residential heating system and compared the energy consumption of residential homes for natural gas, electrical and solar water heaters. Environmental considerations, direct fuel consumption and energy costs of supply are all taken into account for solar water heating of a four-person home in Miami, Florida. Brown et al. indicated that, based on optimal assumptions, a solar water heater can be 114 times more efficient than an electrical water heater and 14 times that of a natural gas heater. Based on the average energy consump-

tion of a four-person home, if all of Florida transitioned to solar water heating systems, an estimated $4.8 \cdot 10^7 \ m^3/year$ of natural gas and $9.5 \cdot 10^6$ barrels of oil per year could be saved.

1.3 Motivation and Objectives

Energy requirements for water and space heating can be drastically reduced through implementation of phase change thermal energy storage. Latent heat storage systems and solar collectors are excellent technologies capable of reducing gas and electricity costs associated with heating applications. As presented above, several design factors influence performance of these systems such as material selection, water heater configuration and type of solar collector. Domestic solar water heaters have the capability to provide residential hot water supplies for 24 hour periods, but further development of efficient systems with appropriate sizing for urban areas is required.

Solar energy systems must take advantage of thermal storage as the incident solar radiation is only available for a portion of the day (this availability is also dependent of weather conditions). Latent heat storage enables solar water heaters to provide energy during night hours, a period of time previously thought to be unusable. This boost in productivity renders solar water heaters more efficient than traditional photovoltaic cells, but require an adequate heat exchange method to aptly harness energy collected. The adaptation of such systems in practical applications is heavily dependent on their higher thermal performance i.e. the collection of solar energy with high thermal efficiency and its transfer to the thermal energy storage and later utilization through highly efficient heat exchange processes.

Decreasing fossil fuel reserves and the detrimental environmental impact of their consumption drive the necessity for a means of highly efficient renewable energy production. With residential electrical and gas applications engulfing the majority of energy usage in North America, solar energy systems should be the scope of current research. Concentrated solar collectors due to their higher efficiencies are more suited solar energy systems, but the sunlight to thermal conversion process needs further efficiency enhancement. This could be achieved by eliminating the intermediate energy conversion process at the receiver of the parabolic dish and transferring the sunlight directly into the thermal energy storage, where the conversion of sunlight to thermal energy occurs at the thermal energy storage interface. Solar energy systems with a latent storage unit, when integrated for domestic use, reduce the need for traditional electrical and natural gas usage and provide a promising reduction of carbon footprints.

The present research aims at addressing some of the challenges associated with the energy harvesting from concentrated solar collectors and integrating it with a thermal energy storage system. The main objectives of the proposed research study are,

(i) To develop a novel "Optical Guide system" for efficiently transporting the radiative concentrated solar energy from the parabolic dish solar collector to the receiver, allowing to eliminate intermediate conventional energy conversion process in the receiver, as well as to minimize other energy losses.

(ii) To develop a theoretical model integrating the parabolic dish collector with a thermal energy storage unit to parametrically investigate the feasibility of this combined system for domestic heating applications.

A schematic of the proposed combined solar collector-thermal storage system is depicted in Fig. 1.6.
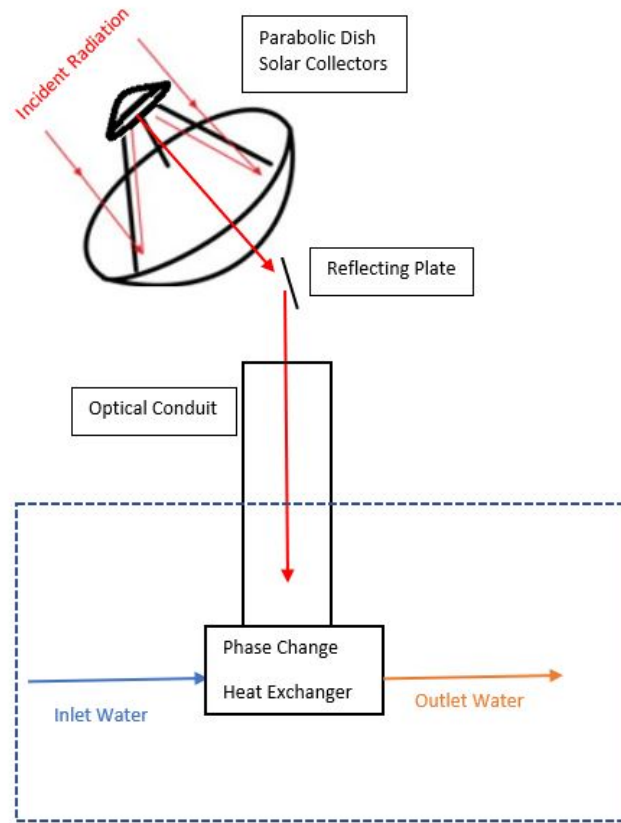
Figure 1.6: Schematic of the proposed integrated solar-thermal storage system for water heating

1.4   Thesis Layout

Introduction, literature reviews, motivation and objectives are included in chapter 1.

Chapter 2 introduces numerical methods used to model the proposed solar collector and novel optical guide, as well as depicts heat flux distributions developed for two ray tracing software programs.

A parametric variation and analysis of the integrated water heating system is computed in Chapter 3 as a framework for future development of latent thermal storage systems.

Chapter 4 summarizes results drawn as well as future recommendations for the advancement of this technology.

Chapter 2

Parabolic Solar Collector Design

Development of an Optical guide to replace traditional thermal receiver at the focal point of Parabolic Dish Solar Collectors requires intensive computational modelling as several factors affect the flux distribution produced by these systems. The optical guide must be placed in such a way that nearly all incident rays are concentrated onto its base, as well as positioned to be non-intrusive to the path of the continuously changing azimuth and altitude angles of the parabolic dish throughout the day. A desirable material for the optical guide must have low absorptivity and high reflectivity to allow efficient transportation of solar radiant energy to the end of the optical guide where the receiver is located. In the proposed design, the conventional receiver at the focal point of the parabolic dish is replaced by a smaller (secondary) parabolic dish to divert the sunlight collected by the primary dish, into the optical guide (see Fig. 2.1).
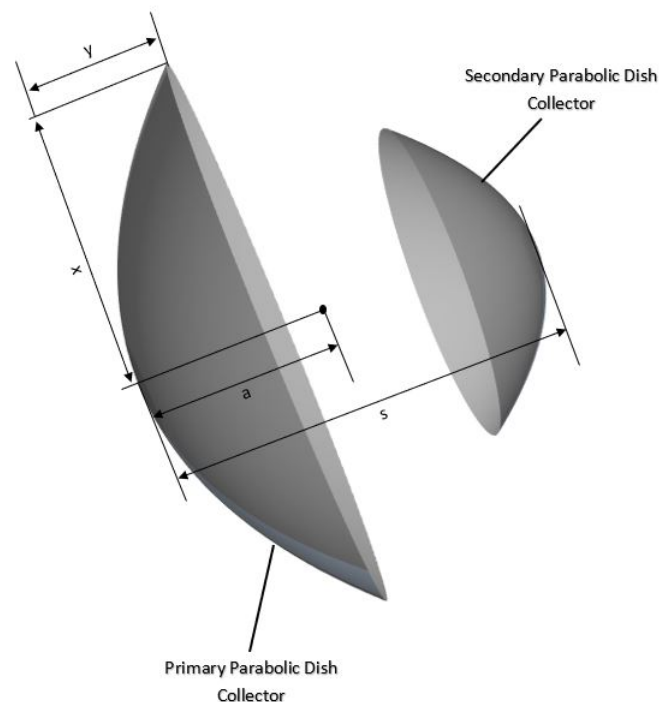
Figure 2.1: Proposed configuration for concentrated solar collector design

To concentrate incident solar radiation, a parabolic dish system must be configured with spe-
cific focal points and spacings to achieve the optimal flux magnitude and distribution. To
achieve this, computational models were designed using various orientations of a two-part
parabolic dish set-up. The dish configurations were used to consider geometric ray optics of
parabolic dishes and flat mirrors before being ray traced using two different software programs.

2.1   Governing Principles

The following section describes basic concepts related to the development and modelling of the
solar collector and optical guide. Radiative heat transfer principles are used to define solution
techniques whereas use of geometrical ray optics are essential for an accurate design of the
numerical model.

2.1.1   Geometrical Optics

Both parabolic dishes are designed using known optical equations for incident rays on curved
surfaces [59]. The equation of a parabolic dish with respect to its focal point, a, and radius, x,
is given as: Eq. 2.1;

$$y = \frac{x^2}{4a} \tag{2.1}$$

Thus, with a desired focal point and radius, the height, y, of a parabolic dish can be determined
(see Fig. 2.1)

As mentioned earlier, the proposed system consists of two parabolic dishes, which serve as
reflective surfaces, creating a direct relation between the focal point of the primary dish and
the distance to the secondary dish defined by Eq. 2.2 [60];

$$f = \frac{f_1 f_2}{f_1 - f_2 - s} \tag{2.2}$$

where the focal distance of the entire system, f, can be computed from the primary focal length
f_1, the secondary focal length f_2, and the perpendicular distance between the reflecting surface
of the two dishes, s, defined by Eq. 2.3 [60].

$$s = f_1 + f_2 + d_o \tag{2.3}$$

The term d_o is derived from the mirror equation, Eq. 2.4 [61] for concave reflectors which
defines the separation from the primary focal point to the secondary focal point needed to
produce concentrated rays at a point, d_i.

$$\frac{1}{d_o} + \frac{1}{d_i} = \frac{1}{f_1} \tag{2.4}$$

Using the above equations, it is possible to design a parabolic dish system with two reflectors
and a desired overall focal length, relative to the separation and focal lengths of the dishes. This

concept is illustrated in Fig. 2.2 and is known as a Gregorian configuration [62]. Gregorian configurations are unique due to their ability to place overall focal points behind the primary reflective surface.
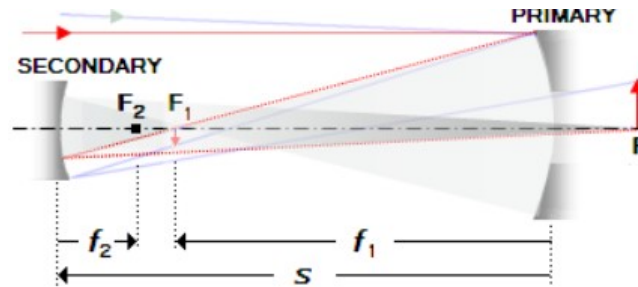
Figure 2.2: Gregorian secondary set-up for parabolic collector system [63]

2.1.2 Law of Reflection

Along with parabolic reflectors, this catoptric system requires a flat mirror to transmit the concentrated solar radiation onto the inner surface of the optical guide. Design and placement of this mirror relies on the overall focal point of the system, and the location of the optical guide. The law of reflection, stated in Eq. 2.5 [60], can be used to determine the angle of orientation for the aforementioned flat mirror to allow for all concentrated rays to be transmitted into the optical guide at any azimuth and altitude angle.

$$\theta_1 = \theta_2 \tag{2.5}$$

Thus for any angle of incidence, θ_1, the flat mirror can be repositioned at some normal to produce the desired angle of reflection, θ_2. This is only true for spectral reflections as diffuse surfaces reflect rays in many directions rather than one.

Incident thermal radiation on a surface is reflected, transmitted or absorbed (see Appendix A1 for illustration) resulting in 2.6.

$$Incident = Reflected + Transmitted + Absorbed$$
$$1 = \rho + \tau + \alpha \tag{2.6}$$

The above dimensionless variables ranging between 0 and 1 are denoted as ρ for reflectance, τ for transmittance and α is the absorptivity of the surface. The power of the reflected ray in ideal spectral reflections is assumed to be the same as the power of the incident ray [64].

2.1.3 Thermal Radiation

Numerical modelling of optical systems is conducted by considering radiative heat transfer methods. Assumptions made for these methods state that all radiation be non-black bodied with perfect spectral reflectance on surfaces, except for the bottom surface of the optical guide (thermal reservoir) which is assumed to be a perfect black body. Radiative exchange between

grey bodies is governed by thermophysical properties at the surface that dictate how much energy is reflected, absorbed or transmitted and depends on factors such as wavelength and temperature. Most of the variables for thermophysical properties are simplified through assumptions, allowing for surfaces to absorb or emit a certain fraction of incoming energy [65]. Derivation of these methods begins with black body radiation.

By integrating Planck's Law for black body radiative intensity over the entire incoming wavelength spectrum, λ, the total blackbody hemispherical emissive power, Eq. 2.7, can be calculated at an absolute surface temperature. In Eq. 2.7, $C_1 = 3.74177153 \cdot 10^{-16}\ W \cdot m^2$ and $C_2 = 1.4387770 \cdot 10^{-2}\ m \cdot K$ are the first and second radiative constants respectively [66].

$$
\begin{aligned}
e_b(T) &= \int_0^\infty e_{\lambda b}\, d(\lambda) = \int_0^\infty \pi\, i_{\lambda b}\, d(\lambda) \\
e_b(T) &= \int_0^\infty \frac{2\pi h c^2}{\lambda^5 (e^{C_2/\lambda T} - 1)}\, d(\lambda) = \sigma T_A^4
\end{aligned}
\tag{2.7}
$$

where σ is the Stefan-Boltzman constant of $5.67 \cdot 10^{-8}\ \dfrac{W}{m^2 \cdot K^4}$ and T_A is the temperature of surface A.

Kirchoffs law for directional total properties states absorbed energy must be equal to that of emitted energy for any real surface in thermal equilibrium. Incorporating thermophysical properties to radiative exchange is accomplished by including the emissivity of surface, ϵ_A, to Eq. 2.7 to find total hemispherical emissive power of a non-black body [67].

$$
E_A(T_A) = \int_0^\infty \epsilon_A e_{\lambda b}\, d(\lambda) = \epsilon_A \sigma T_A^4
\tag{2.8}
$$

A radiative interchange factor must be determined to compute non-black body radiative heat transfer between surfaces. This factor, $B_{i \to j}$, is the fraction of emitted energy from a surface i, absorbed by surface j and is a geometrical relationship between the two surfaces [68]. Eq. 2.9 describes the radiation exchange between emitter surface A_1 and absorptive surface A_2.

$$
E_{A_1 \to A_2}(T_{A_1}) = A_{A_1} B_{A_1 \to A_2} \epsilon_{A_1} \sigma T_{A_1}^4
\tag{2.9}
$$

where the $B_{i \to j}$ term indicates the energy emitted by surface A_1 onto A_2, including all other energies that may have been reflected from A_1 onto A_2. Simple geometries such as planes and cylinders have readily available factors documented, while for complex geometries, computer programs have been developed to calculate radiative interchange factors.

Directional spectral absorptivity (Eq. 2.10) defines the fraction of incident power absorbed, $d^3 P_a(\lambda, T_A, \theta_i, \varphi_i)$, by the intensity of incident radiation at that wavelength domain and direction, $i_{\lambda,i}(\lambda, \theta_i, \varphi_i)$ [69].

$$
\alpha(\lambda, T_A, \theta_i, \varphi_i) = \frac{d^3 P_a(\lambda, T_A, \theta_i, \varphi_i)}{i_{\lambda,i}(\lambda, \theta_i, \varphi_i)\, dA\, cos\theta_i\, d\Omega_i\, d\lambda};\ \ d\Omega = sin\theta\, d\theta\, d\varphi
\tag{2.10}
$$

where $d\lambda$ is the wavelength interval, dA is the considered differential surface element, $d\Omega_i$ is the differential solid angle and θ_i, φ_i refer to directions with i subscript representing incidence. It should be noted that T_A refers to the surface temperature of the absorbing element in this case. A representation of the directional spectral absorptivity can be found below in Fig. 2.3, where n and t represent normal and tangential coordinates respectively.
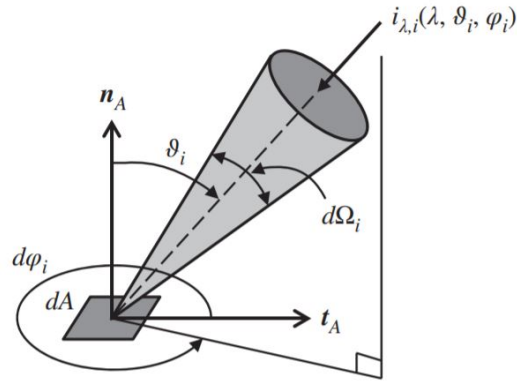
Figure 2.3: Schematic of directional spectral absorptivity [70]

2.2   Tracer Modelling

Tracer^{TM} is used in the present study. It is a pythonic ray-trace engine used to determine heat flux distributions produced by solar energy applications [38]. Creation of ray traced scenes is done through modelling of a surface with Tracer^{TM}'s geometry manager, which allows the user to define various 3D and 2D objects such as cylinders, parabolas and flat plates. Once an object is defined through the geometry manager, the user specifies its location on a three-dimensional Cartesian coordinate system. This allows for creation of assemblies of several objects in a scene relative to one local coordinate system. Objects are defined with a user input absorptivity as well as an optic manager; allowing for further specification of reflective properties such as one-sided mirrors and Lambertian (matte) reflectors. The incoming heat source is a modelled sun shape that disperses ray energy to each ray equidistantly from a user defined location, shape and intensity. Iterations on Tracer^{TM} are set through the program and only display results once a converged solution is determined.

Capabilities of Tracer^{TM} include creation of flat, parabolic and conical surfaces with sun-shape implementations that can be analysed with a dedicated toolbox to track rays that hit a surface and associated fluxes. In the present study, Tracer^{TM} was used to model the optical guide system by creating two parabolic dishes oriented to direct incident radiation into an optical guide. The dishes were programmed using Tracer^{TM}'s in-house libraries and computationally rendered with Coin3D^{TM} and Pivy^{TM}; pythonic rendering toolkits. Tracer^{TM} contains no GUI and uses python math libraries as well as NumPy^{TM} and SciPy^{TM} to define arrays within the program and perform Monte-Carlo Ray Trace algorithms. Objects created in the environment have applied to them a mesh of user defined accuracy, dependent on the simulation requirements. Distances between dishes as well as the parabolic equations associated for Tracer^{TM}

were determined through classic optical equations and properties of parabolic reflectors. This creates a highly defined environment that can model complex optical systems with a user defined solar intensity and material optical properties. Using this program, it is possible to model a preliminary optical guide with its respective parabolic dish solar concentrator. Tracer™ is used to numerically compare results of this solar concentrator to that of another ray tracing program, SolTrace™, in order to provide confidence on current design methods.

2.2.1   Monte Carlo Ray - Tracing

Tracer™ uses Monte Carlo Ray Tracing (MCRT) to depict ray paths coming from a user defined directionality, intensity and sun shape as they undergo spectral reflections. MCRT is accomplished by means of Monte Carlo integration, where random points of a function are sampled and averaged over an integration domain [71]. This type of integration provides a fast method of stochastic sampling to approximate equations that would otherwise be impossible to analytically compute.

MCRT is accomplished by using the Monte Carlo algorithm to integrate over all the illuminated ray paths on a single point defined in the environment. These ray paths are then reduced by a bidirectional reflectance distribution function (BRDF) which determines how much energy from that ray path is transferred to another surface; and is repeated for every surface element on the ray traced grid [72]. This ray trace algorithm views the directional spectral absorptivity (see Eq. 2.10) as the probability of an energy bundle being absorbed in interval $d\lambda$ and direction θ_1. Knowing the direction of the ray, the MCRT algorithm for Tracer™ can be described in the following steps:

1. Choose a ray given with weight equal to 1.

2. Trace ray to find point of intersection with the nearest surface.

3. Randomly decide whether to compute emitted or reflected light. This is a user defined variable.

3A. If emitted, return weight of emittance (0-1).

3B. If reflected, return weight of reflectivity (0-1).

4. Randomly scatter the ray according to the BRDF (bidirectional reflectance distribution function).

5. Repeat Step 2 for the number of user defined rays.

By sending several primary rays and tracing the recursive secondary rays, a scene can be computationally rendered depicting the exact reflections produced by incident sun rays with a user defined intensity assigned to each ray. Defining absorptivity, emissivity and reflectivity of each surface allows the Tracer™ program to accurately assign each surface element a heat flux according to the number of rays that strike, as well as reduce the energy of a ray that has already been reflected by a factor of its aforementioned defined properties. Ray tracing programs use this method to define heat fluxes on surfaces, but require additional sub-routine programming to calculate local temperatures of intersected surfaces.

2.2.2 Proposed Design

To meet design objectives, the proposed solar collector system consists of a Gregorian secondary reflecting configuration along with an optical guide and a concentrated solar energy receiving surface at the bottom of the optical guide (thermal reservoir). To accomplish this, two parabolic dishes are modelled in an environment containing a flat reflecting plate at the overall system focal point with a cylindrical tube placed beneath it (see Fig. 2.4). Symbols used to refer to the proposed design's components are listed in Table 2.1.

Table 2.1: Description of referred to components of the parabolic solar dish collectors and optical guide

Reference to Proposed Design	Component	Description
Solar Collector	A	Primary Parabolic Solar Collector
	B	Secondary Parabolic Solar Collector
Optical Guide	C	Reflecting Flat Plate
	D	Optical Conduit
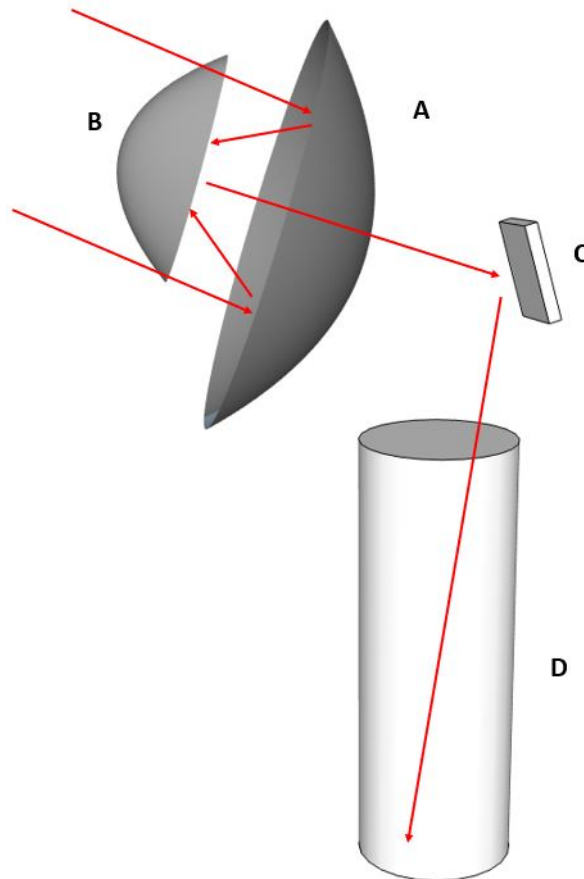
Figure 2.4: Proposed schematic of parabolic concentrating solar collector system with optical guide

The concentrated solar ray bundle collected at the bottom of surface D, the optical conduit, defines the radiative flux distribution theoretically imposed on the surface of the concentrated solar energy receiver. The collected intensity can be altered by varying distances between components, allowing for several distributions of flux to be achieved. Dimensions between each component as well as their respective angle of orientation throughout the day must be carefully defined in order to accurately model the collected overall flux distribution.

Due to the complexity of the charging and discharging processes, ideal flux distributions for the input heating condition of PCM thermal energy storage is not currently known. Once further research is conducted in the above mentioned field, this modelling technique can be used to determine the appropriate dimensions and locations of components to produce a desirable flux distribution. The system component that will receive the thermal energy from the sunlight and transfer this energy to the PCM thermal storage must be further studied as current knowledge in this field is scarce. Hence, in the present research, an overall efficiency of this solar thermal to PCM storage transfer process is assumed to account for potential losses that would occur in this process.

2.2.3   Solar Collector Modelling

For preliminary purposes a 1/3 scaled version of the Solatron© solar dish collector was modelled (see Appendix B1 for dimensions and illustration of industrial Solatron model). The initial diameter and focal point (f_1), for the primary solar collector, component A (see Fig. 2.4), were chosen to be 3m and 1m respectively. Using Eq.2.1, the parabolic dish can be defined in Tracer^{TM} using Python^{TM} math libraries as a function of x and y. Diameter was chosen for initial design purposes but is intended to be altered in future design considerations. The primary collector diameter governs collected incident radiation, thus a larger primary dish will ultimately produces more usable energy than a smaller dimensioned dish. Although larger dishes will collect more solar insolation, the energy requirements to preform solar tracking as well as spatial restrictions can limit their overall size. By defining a primary focal point, f_1, and a secondary focal point, f_2, use of Eq. 2.3 yields the spacing between two parabolic reflectors, S (see Fig. 2.5).
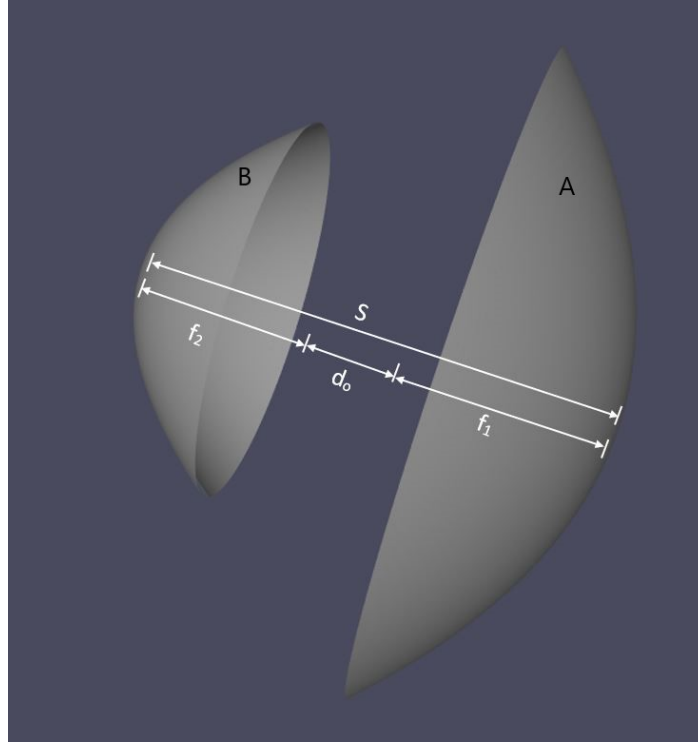
Figure 2.5: Schematic of proposed solar collectors with spacing denotations

A secondary dish, component B, was designed to be non-obstructive to incident solar radiation and create an overall focal length that is behind the aperture of the primary dish (see Fig. 2.2) and allows for redirection of solar energy by means of flat mirror reflection. Larger secondary collectors will produce a larger shadow over the primary dish, blocking insolation at that location. Reducing the secondary dish size has the potential for solar radiation concentrated by the primary collector to miss its extremities, reducing system efficiency. This led to the design of component B, the secondary dish (see Fig. 2.4), being an approximately 1/4 scaled down version of the primary dish, with a diameter of 0.7m and a focal length of 0.2m; programmed into Tracer^{TM} similarly to that of the primary dish using Eq. 2.1.

Perpendicular distance between the two dishes, s, was calculated through the use of Eq. 2.2 and Eq. 2.3, and was determined to be 1.25m to ensure ray bundle concentration at a desirable location behind the primary dish. The secondary dish must be placed past the focal points of both dishes with respect to the d_o value due to scattering of rays at the initial system focus. Increasing the value of d_o will create a farther focal point, while decreasing this value will produce a closer overall focal point and ultimately affects the distribution of flux produced in the optical guide as it can will be finely, or coarsely concentrated, dependent on this term.

2.2.4 Optical Guide Modelling

The optical guide must accomplish design key requirements for maximum radiative energy transfer between the incident concentrated ray bundle and the receiving surface. Solar dish collectors must track the sun in both azimuth and altitude angles, thus the optical guide must account for spatial constraints of the tracking system as well as accommodate various angles

of incidence for concentrated ray bundles. This means the optical guide must be small in size relative to the primary reflecting dish, as well as have the ability to freely redirect rays based on tracking orientation. The proposed optical guide is a unit consisting of two parts, a flat mirror and an optical conduit (see Fig. 2.4). The flat mirror is placed at the overall system focus and be used to redirect concentrated rays into the bottom of the optical conduit. A receiving surface at the end of the conduit will absorb the radiant energy and transfer it to the PCM thermal storage via heat conduction.

To evenly direct the concentrated ray bundle, a flat mirror (component C) is placed at the overall system focal point, f, located 0.44m behind the primary dish (component A). This distance is determined using Eq. 2.2 and orientated to θ_r depending on the angle of solar incidence calculated by The Law of Reflection, Eq. 2.5 (see Fig. 2.6).
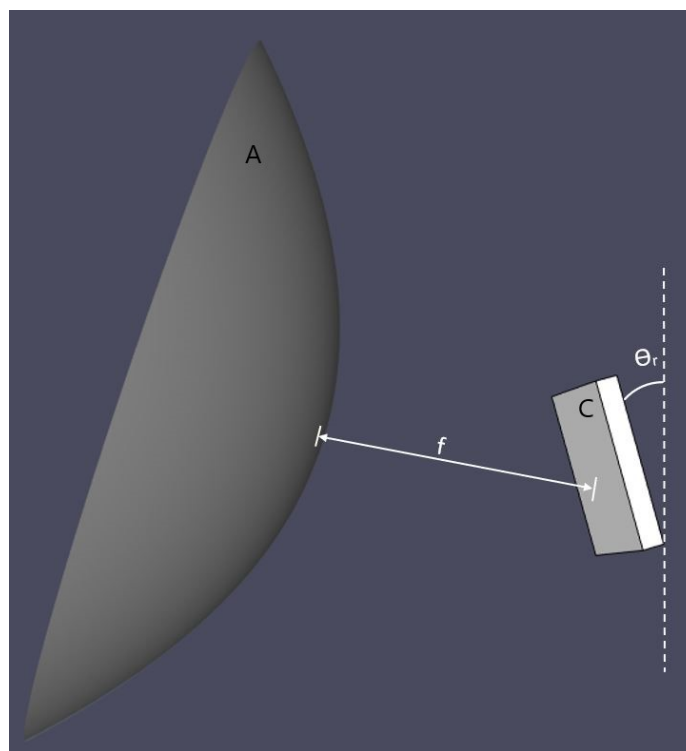
Figure 2.6: Reflecting plate location with respect to primary dollector dish and angle of orientation

Angle of orientation of the flat mirror is dependent on the altitude angle of the solar collector as its functionality is to direct rays into the optical guide and must be repositioned accordingly. The flat mirror will be rotated such that incident rays are reflected at an angle of 25° below the mirror's normal. An example of this is the placement of the mirror at 60° with respect to the global coordinate system to redirect concentrated rays for solar collector altitude angle of 35° (see Eq. 2.5). Rotating the mirror in this manner ensures ray placement into the optical conduit underneath, regardless of altitude angle. Placement and orientation of this flat mirror ensures a relatively symmetrical distribution of the radiant flux at the bottom receiving surface of the optical conduit; but can be repositioned to produce various heat flux contours for multiple

applications. Modelling of the optical guide in this manner allows for consistent theoretical prediction of flux profiles that are expected to be generated for several angles of incidence. The repositioning of the mirror will induce a higher or lower focus of concentration on the bottom of the optical conduit, component D, impacting the way radiant flux is distributed at the receiving surface, and hence the energy transferred to the thermal storage. Placement of this mirror is crucial as the concentration of sunlight at the receiver surface may produce vary high heat flux, which with resulting high temperatures, could be detrimental for the receiving surface material. On the other hand, a lower concentration of flux distribution may lead to a lower overall system performance at the benefit of material integrity.

Altering the angle of the flat mirror with respect to the varying azimuth and altitude angles will direct reflected ray bundles to the same location, thus an optical conduit can be placed accordingly underneath the catoptric system such that all reflected rays strike the surface of the conduit and are absorbed by the receiving system. For ease of manufacturing, this conduit was chosen to be cylindrical in shape. Preliminary length of the optical conduit was chosen to be 1m to allow for sufficient space underneath the primary dish in terms of rotational tracking clearance, while the diameter is proportional to the dimensions of the flat mirror to allow for plate rotational tracking. Due to the flat mirror being placed at the overall system focal point, the rays are concentrated on a small surface area of the flat mirror. A very large flat reflecting plate will be intrusive to the systems tracking process, while a small plate may not fully reflect every ray in the concentrated bundle for all angles of incidence. Dimensions of the flat plate, component C, will be an infinite reflective plane that does not extrude past other components in the environment until approximate size of concentrated ray bundle can be determined in order to optimize its size. Diameter of the optical conduit will determine whether or not the incident solar rays will reflect inside of it as ray bundles spread radially after reflection from a flat plate.

To determine initial optical conduit diameter, an estimation of 0.34m is made. A diameter of this magnitude is approximated as a guideline test condition to determine flux distributions that will develop on the receiving surface at the entrance of the thermal reservoir. A larger diameter conduit will be capable of retaining a spreading bundle of rays at longer lengths compared to that of a narrower conduit; thus will produce a lower concentration of flux at the receiving surface as more rays are located at the extremities of the conduit (see Fig. 2.7). An optical conduit of lesser diameter will naturally produce a higher flux concentration due to its reduced area, but realistic thermal losses may be increased as a result of spread rays being absorbed by the internal conduit surface. Dimensions of the optical guide are to be later iterated to produce the most favourable radiant flux distribution at the receiving surface.
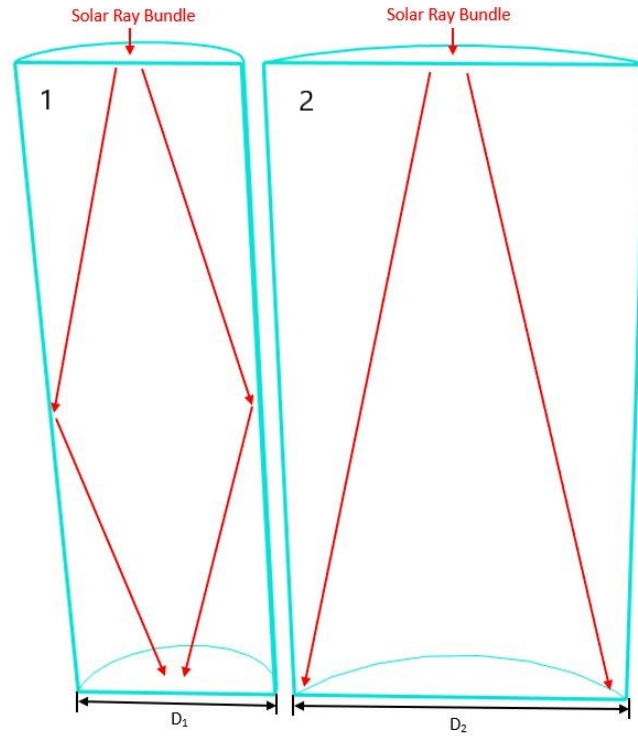
Figure 2.7: Theoretical cross sectional representation for optical conduits of different diameters and verbatim length subjected to ray bundle spread with $D_2 > D_1$

2.3   Tracer Results

Tracer^{TM} interprets the energy associated with each ray to the incident surface and calculates a flux distribution on receiving surfaces from that data. The in-house interrogation methods allow Tracer^{TM} to relay ray energies calculated through Monte-Carlo simulation onto surface nodes and output this data to an Excel^{TM} file for analysis. The magnitudes associated with Tracer^{TM}'s calculated flux distribution is related to the nodal size of mesh used in the environment, number of incident rays and the energy intensity, all set by the user. Tracer^{TM} will distribute the user defined number of rays equidistantly across an area and directional vector in the scene, both set by the user. This program however, is not capable of calculating conductive or convective heat transfer in the environment, thus the only flux that can be calculated is that developed radiatively on the surfaces. Results are calculated from fully reflective surfaces with the exception of the bottom of the optical conduit (also referred to as receiving surface) which is fully absorptive.

A preliminary energy balance was performed to confirm the accuracy of Tracer^{TM} programming for initial numerical modelling. In order to reduce truncation error, a grid independence test was conducted, where the overall mesh of the catoptric system as well as the number of rays tested were refined through several iterations until energy calculations showed no deviation. Once the numerical model was confirmed, the parabolic dish system was tested at various altitude angles to demonstrate the optical guides ability to reflect concentrated sun rays into the

desired location for several orientations.

2.3.1 Energy Balance Validation

A basic energy balance was completed to validate the ability of Tracer™ to compute radiative energy transfer from one surface to the next. The initial test consisted of two flat mirrors with incident rays striking and reflecting off one plate onto the other (see Fig. 2.8). Various properties were changed to validate Tracer™'s capabilities and are described in further detail in this subsection. The preliminary energy balance consisted of two rays, N, at a total incoming flux $F = 1000 W/m^2$, over a surface area of $A = 100m^2$. Tracer™ then assigns each outgoing ray an energy, E, based on the above-mentioned variables as;

$$E = \frac{F A}{N} \tag{2.11}$$

For the initial two mirror set-up, two rays were used and reflectivity of these mirrors were varied to judge accuracy of results over a wide range of variables. Using MCRT, Tracer™ assigns each surface an energy based on the number of rays that strike it. For these energy balances, every ray strikes each surface once allowing for simple calculations of expected absorbed energy on both surfaces. Using Eqn. 2.11 and Tracer™ interrogation methods, tests were conducted for different absorptivity and reflectivity values of the two surfaces and the results are presented in Table 2.2.
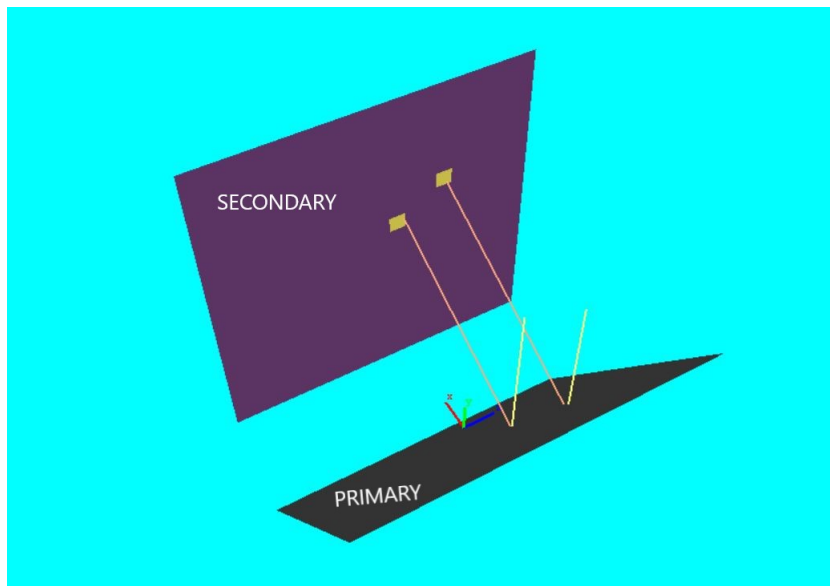
Figure 2.8: Initial two-mirror energy balance using two incident solar rays of equal intensity

Table 2.2: Initial energy balance between primary and secondary mirror of varying reflectivity and absorptivity

Test	Mirror	Absorptivity	Reflectivity	Tracer Total Energy Flux [W]	Theoretical Total Energy Flux [W]
1	Primary Mirror	0	1	0	0
	Secondary Mirror	1	0	100,000	100,000
2	Primary Mirror	0.5	0.5	50,000	50,000
	Secondary Mirror	0.5	0.5	25,000	25,000
3	Primary Mirror	0.25	0.75	25,000	25,000
	Secondary Mirror	0.25	0.75	18,750	18,750
4	Primary Mirror	0.25	0.75	25,000	25,000
	Secondary Mirror	0.50	0.50	37,500	37,500
5	Primary Mirror	0.25	0.75	25,000	25,000
	Secondary Mirror	0.75	0.25	56,250	56,250

Table 2.2 depicts a difference of energy between tests based on absorptivity and reflectivity, and is accurately calculated by Tracer[TM] for every situation. The above agreement in data provides confidence in Tracer[TM]'s capabilities of transferring ray energy to different surfaces at various absorptivities, but further testing was conducted to confirm this attribute at higher ray counts. Analogous modelling and variable manipulation to that of the above energy balances were conducted with 20, and 500 rays depicted below in Fig. 2.9.

(a) 20 Rays
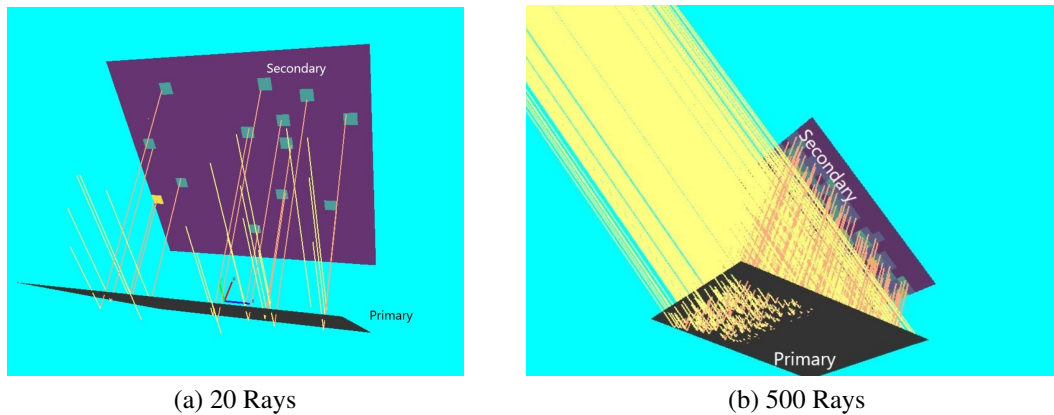
(b) 500 Rays

Figure 2.9: Two-mirror energy balance with primary and secondary mirror both receiving 20 and 500 rays

The predicted values of energy for both mirrors in each case were congruent to that tabulated above in Table 2.2. This is due to every ray striking both mirrors in all scenarios with no absorptive disruption, producing the same total energy dependent on analogous reflective properties. Comparing the surface of the secondary mirror in Fig. 2.8 and the 20 ray simulation of Fig. 2.9a it is obvious the differences produced in these tests are the distribution of flux developed

locally on the mirrors. Further analysis of Fig. 2.9b shows that the flux distributions will be more refined with a higher ray count. Conclusively since Tracer$^{\text{TM}}$ divides the total input energy by the amount of rays, the number of rays used does not affect power absorbed, granted the same percentage of rays strike the receiving surface.

2.3.2   Grid Independence Tests

Tracer$^{\text{TM}}$'s input ray count is significant for scenarios with obstructing objects as each ray carries equal energy; thus a single blockage on a lower ray count simulation results in greater discrepancies of flux than its counterpart with more rays. Since solutions of flux distribution vary with grid density as well as ray count, a validation to eliminate truncation error must be conducted to ensure that the computational results are independent of the grid and number of rays. To accomplish this, a grid independence test was conducted to compute the optimal mesh size and number of rays. This was done by simulating the solar dish collector for different numbers of incident rays and analysing the associated flux distributions on an absorptive surface of the system. Incident rays were concentrated in the fully reflective, Gregorian optical guide system where the average radiative heat flux on a receiving plate at the bottom of the optical conduit was calculated. Tracer$^{\text{TM}}$ conducts a simulation using Monte Carlo algorithms and user defined datum for input conditions to construct this environment, allocate a fraction of total energy to each ray and calculate the flux distribution on an absorptive surface. Figure 2.10 depicts the numerical model used for the grid independence test.
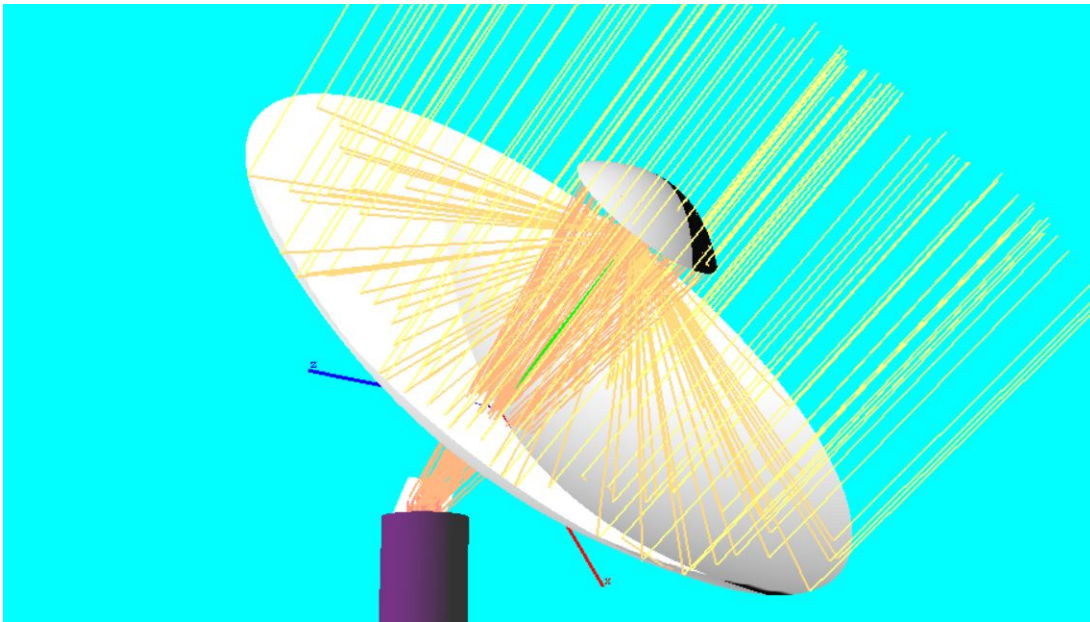
Figure 2.10: Tracer modelled parabolic dishes and optical guide with incident rays oriented at an altitude angle of 45°

Average flux is based on the absorptivity of materials of the system, and the optical conduit's 2D quadrilateral mesh distributed in an o-grid. Increasing nodal count increases the number of data points collected, which in turn provides a smoother sample curve with a more accurate

representation of flux on that surface. Mesh density was refined to provide the most accurate solution for this simulation while remaining in the limits of computational efficiency. For modelling purposes, each surface was fully reflective with the optical conduit being fully absorptive to assume minimal losses. The ray count was refined to account for shading from the secondary dish. Shading is crucial for truncation error as total flux is distributed evenly between each ray; allotting a greater value of flux to a smaller ray count. This leads to simulations with smaller ray counts to have lower overall surface fluxes, ultimately skewing numerical results. Figure 2.11 depicts the grid and ray independence test results at an incoming flux of 1,360 W/m^2 based on the solar constant, the average radiative intensity of the sun [73]. Table 2.3 lists the above mentioned data points.
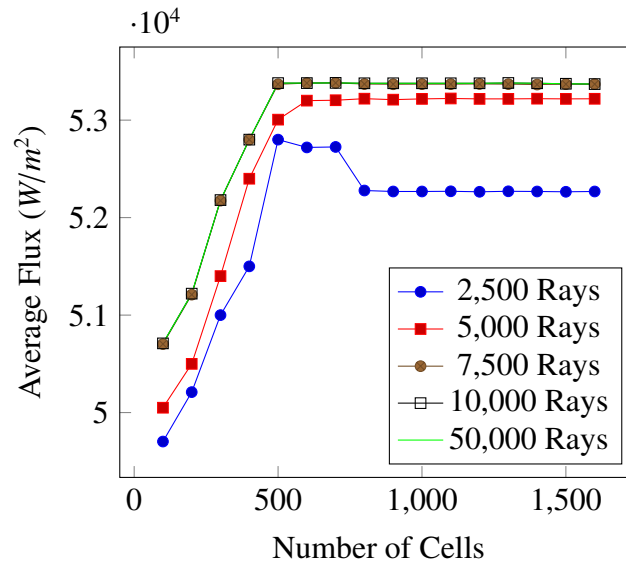
Figure 2.11: Graphical depiction of grid and ray independence tests based on average flux collected in the bottom of the optical conduit

These results indicate high variation for the lower ray counts. This is due to a higher percentage of rays striking the bottom of the optical conduit in simulations with a higher ray count. Within the ray counts of 7,500 - 50,000, over 75% of incident rays were absorbed and solutions varied by less than 1%; allowing an acceptable ray count for future simulations to be within that domain (see Table 2.3).

A major downfall of the Tracer™ program arises when computing a trace with more than 50,000 rays as it runs into several compiling errors such as failing to computationally render and accurately map ray intersections. Running simulations at 50,000 rays results in longer computational times with slower rendering speeds for virtually the same result as traces with the ray count of 10,000. Additionally from Fig. 2.11 it is apparent the solution for the aforementioned ranges also remains consistent regardless of mesh sizes over 500 cells. This is due to the simplicity of the geometric surface being tested. A planar surface requires much less cells for computation than if the recieving surface had been a 3D object. For receiver geometries based on these validations, it is reasonable to set parameters of future simulations to an appropriate ray count of 10,000 and mesh size of approximately 1,000 cells.

Table 2.3: Tabulated grid and ray independence tests based on average flux collected in the
bottom of the optical conduit

Number of Cells	Average Flux [W/m^2]				
	2,500 Rays	5,000 Rays	7,500 Rays	10,000 Rays	50,000 Rays
100	49,703	50,050	50,703	50,710	50,710
200	50,210	50,500	51,210	51,220	51,220
300	51,000	51,400	52,174	52,180	52,180
400	51,500	52,399	52,800	528,00	528,00
500	52,800	53,005	53,368	53,380	53,380
600	52,720	53,200	53,380	53,380	53,380
700	52,725	53,204	53,382	53,382	53,382
800	52,278	53,220	53,370	53,378	53,378
900	52,268	53,210	53,368	53,378	53,378
1000	52,268	53,218	53,369	53,378	53,378
1100	52,270	53,222	53,369	53,378	53,378
1200	52,265	53,218	53,371	53,378	53,378
1300	52,270	53,218	53,369	53,381	53,381
1400	52,268	53,220	53,365	53,378	53,378
1500	52,265	53,218	53,369	53,373	53,373
1600	52,268	53,219	53,369	53,370	53,370

2.3.3   Flux Distributions at Various Incident Angles

Solar dish concentrators must track the sun at various attitude angles in order to produce the
highest possible radiative flux. Hence, one design specification for the optical guide is to
be able to move with the tracking system and produce a consistent flux distribution on the
receiver surface, in every tracked angle. To accomplish this numerically, the geometry in Fig.
2.10 was modelled based on geometrical optics (see Section 2.2) at various altitude angles
while changing the orientation of the flat mirror based on the law of reflection. The data for
the reflecting plate provided indicated the coordinates of rays that intersected this component,
allowing for trimming of reflecting plate that was not intersected. The area of reflecting plate,
component C, intersecting incident rays was found to have an effective height and width of
0.35m and 0.225m respectively. From previous validations, a nodal concentration of 1000
cells with 10,000 rays and an incoming flux of 1,360 W/m^2 equal to that of the solar constant
were chosen. Table 2.4 lists the total average flux produced on the fully absorptive receiving
surface at the bottom of the optical guide after each ray has intersected with the fully reflective
dish and flat mirror elements.

Table 2.4: Tracer average absorbed flux at the receiver surface for various altitude angles

Dish Altitude Angle	Average Flux [W/m^2]
45°	53,378
55°	52,925
65°	52,530
75°	52,530

The design of the optical guide includes repositioning of the flat plate to be oriented accordingly to the angle of incidence of the primary dish. Placement of the components in the computational environment as well as proper ray count and cell number produces flux distributions for every altitude position within a 10% difference range. Tracer^{TM} cannot conduct simulations with larger ray counts and often runs into computational errors rendering it limited to the accuracy and reliability of its solutions. This data reinforces the mathematical modelling used as the rotation the of angle of orientation of flat plate mirror with respect to insolation angle, described in Section 2.2.4, resulted in a consistent average absorbed flux regardless of altitude angle, but are of lesser importance when considering detail in flux distribution.

2.4   SolTrace

SolTrace^{TM} will be used for comparison of results computed by Tracer^{TM} as it is a reliable software program that has shown high accuracy in radiative ray trace modelling. SolTrace^{TM} is a free to use optical simulation tool developed by the National Renewable Energy Laboratory (NREL) created specifically to model and calculate optical performance of concentrated solar collectors. SolTrace^{TM} contains a GUI and is based off C++ coding and utilizes Monte-Carlo Ray Tracing to perform simulations (see Section 2.2.1). Modelling in SolTrace^{TM} consists of user defined stages within a global coordinate system. Stages are optical elements that are used to track rays as they pass, as if a ray leaves a stage it will not return to that stage along its entire path through the system. Stages consist of elements, which are defined surfaces containing optical properties and interactions and can potentially alter ray trajectory. Surface contour options available in SolTrace^{TM} are various types of surfaces of revolution ranging from planes to spheres and cones. All input data are entered alphanumerically through a form on the SolTrace^{TM} program that can also be entered through spreadsheet format.

The sun is defined as an energy source by two parameters; its position as a point relative to the global coordinate system and the intensity distribution across the sun's diameter, known as sun shape. Its position is defined as a point in space where a vector from this point to the global coordinate system origin defines the sun direction. The radial intensity across the sun can be selected from three options of probabilistic distribution (see Appendix C1 for sun shape illustration). Gaussian and pillbox sun shapes are commonly used in concentrated solar power simulations, while the third option for sun shape is a user defined set of datum points for intensity distribution [74]. Gaussian sun shapes incorporate solar intensity deviation while pillbox shapes are evenly distributed, but neither mimic the true nature of earth's sun as sun shape varies based on location, weather conditions and time. Pillbox distributions are adequate for a large domain of numerical simulations [74]. SolTrace^{TM} has readily available user guides

and developer reports on features of the program and will be compared to results depicted from the Tracer[TM] ray trace engine to validate solutions and provide confidence in the design process.

2.4.1 SolTrace Modelling

Calculations for ray energies based on reflections are similar to that of Tracer[TM]. When a ray intersects a surface, SolTrace[TM] computes which side of the surface is struck and then applies the appropriate optical property to determine further interactions. If the ray is computed as absorbed by the Monte-Carlo Ray Trace algorithm (see section 2.2.1), SolTrace[TM] applies the energy from that ray to the incident surface and moves onto the next ray. If the ray is reflected, SolTrace[TM] computes and averages parallel and perpendicular polarizations to determine the reflected fraction.

For the purposes of optical guide numerical modelling, all rays are assumed to be striking a surface with no transmitted energy. A more precise method of calculating absorption utilizing path lengths and material properties does not exist, rendering the accurate modelling of optical properties for stage elements crucial. SolTrace[TM] modelling consisted of development of a similar simulation to that conducted using Tracer[TM]'s ray trace engine. Using analytical methods described in Section 2.1 a SolTrace[TM] model was created with parameters described in Table 2.5.

Table 2.5: SolTrace Ddesign dimensions, locations and description of components

Object	Surface Contour	Size Parameters	Location
A) Primary Reflector	Parabola	Outer Diameter = 3m Inner Diameter = 0.46m Focal Length = 1m	x = 0 y = 0 z = 0
B) Secondary Reflector	Parabola	Outer Diameter = 0.7m Focal Length = 0.2m	x = 0 y = 0 z = 1.25m
C) Flat Mirror	Rectangular Plate	Height = 0.35m Width = 0.225m	x = 0 y = 0 z = -0.44m
D) Optical Conduit	Cylinder	Diameter = 0.34m Height = 1.1m	x = 0.35m y = 0 z = -1m

This model is identical to the simulation produced in Tracer[TM] and will be used to validate the placements and energy calculations produced by Tracer[TM]'s ray trace engine. A depiction of this initial numerical model created by SolTrace[TM] and displayed at 45° can be found in Fig. 2.12.
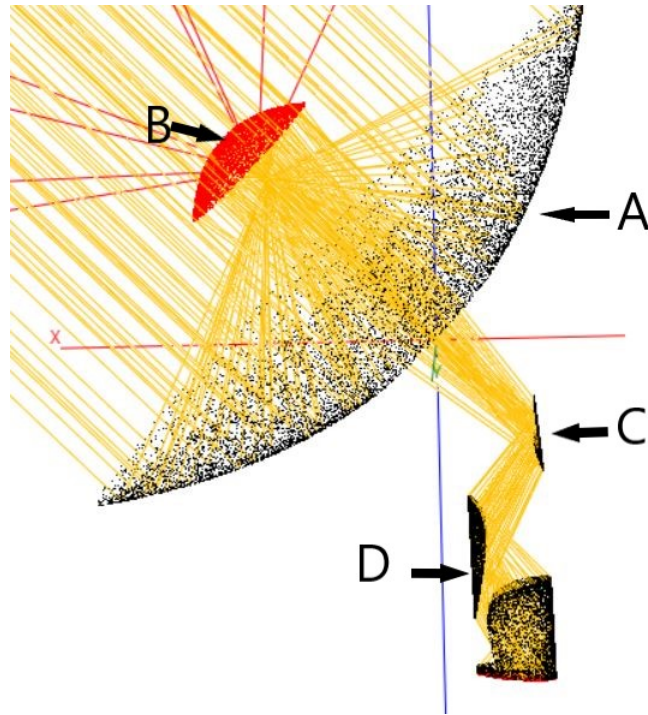
Figure 2.12: SolTrace initial numerical model of concentrated solar collector with optical guide denoted in Table 2.5

SolTrace^{TM} only shows the surfaces struck by incoming or reflected rays, thus elements will not be fully computationally rendered in areas that are not intersected by any ray. Rays coded red depict paths of rays that do not intersect with any other elements in the stage. All surfaces are fully reflective, with no transmission or absorption taking place with the exception for the bottom of element D, which is fully absorptive.

2.5　SolTrace Results

Defined systems are traced with a number of rays input by the user. Number of rays for simulations depends on the required analysis as fewer rays can still provide accurate results for specific scenarios in SolTrace^{TM}. The National Renewable Energy Laboratory documentation provides ray trace parameters for various simulations eliminating the need for ray and grid independence tests for preliminary SolTrace^{TM} validation[74]. From NREL documentation, to simulate a detailed radiant energy map in the optical guide, a ray count of 1,000,000 is required. This is due to the complexity and detail required for an accurate radiant energy contour; whereas only 10,000 rays will be required to solely calculate the average efficiency of optical receivers [75]. Simulations that do not require detailed flux maps can be done at a lesser ray count to reduce the computational time while still yielding accurate results.

SolTrace^{TM} can display results through 3D scatter plots of elements with ray intersections or radiant flux maps on planar surfaces; while statistical information such as peak and average fluxes as well as uncertainties can be saved onto a file for processing. Results provided from SolTrace^{TM} depict a higher resolution of flux distribution to that of Tracer^{TM} due its ability

to generate a greater number of rays; making it more accurate in computing absorbed radiant profiles at the reservoir entrance. The initial numerical model depicted in Fig. 2.12 was varied in altitude angle for an operating range between 30° and 75° with the flat mirror's orientation being changed according to the Law of Reflection (see Section 2.1.2). Results for this range of data are presented in Table 2.6.

Table 2.6: SolTrace average flux developed at the receiver surface located at the bottom of the optical conduit, at various altitude angles

Dish Altitude Angle	Average Flux $[W/m^2]$
30°	61,050
35°	61,147
40°	61,179
45°	61,182
50°	61,228
55°	61,361
60°	61,145
65°	61,313
70°	61,148

These values depict the radiant flux at the bottom of the optical guide with a 1,000,000 ray count simulation with no conductive or convective heat transfers, at an intensity equal to the solar constant. Values are consistent within 1% of each other between altitude angle variations, indicating that the proposed geometric configuration consistently transfers the radiant energy from the sun to the receiver surface at different altitude angles.

The optical guide must direct light to the bottom of the optical conduit and develop some flux distribution that will effectively be transferred as thermal energy to the PCM storage. The desired flux distribution may vary with thermal storage applications depending on the geometry and configuration of the thermal energy storage, but the current distribution calculated in the initial SolTrace$^{\text{TM}}$ modelling provides deep insight on design methodology. The simulated radiant flux distribution is dependent on the shape and orientation of the reflecting mirror as well as the optical guide; thus adjustments can be made to the current design to accommodate for any desired radiant flux distribution at the bottom of the optical guide. Figure 2.13 depicts flux distribution for the dish altitude angles of 30°, 40°, 50° and 60°.

Although the average flux depicted in Table 2.6 does not change significantly, it is evident through Fig. 2.13 that flux distribution alters drastically throughout altitude angles. The diameter of the distribution remains a constant 0.30m for all variations, but local fluxes can be seen moving from left to right as altitude angle increases. This variation in flux distribution is due to incident sun rays striking at inclined angles as it moves from east to west and the flat mirror's orientation relative to the law of reflection. With alteration of the flat mirror's orientation, it is possible to produce several different flux distributions that can be maintained as the altitude angle changes throughout the day. If a suitable flux distribution is determined through further research, modelling techniques will be able to closely mimic the desired profile using the aforementioned techniques.

(a) 30° Altitude Angle Flux Distribution

(b) 40° Altitude Angle Flux Distribution

(c) 50° Altitude Angle Flux Distribution

(d) 60° Altitude Angle Flux Distribution
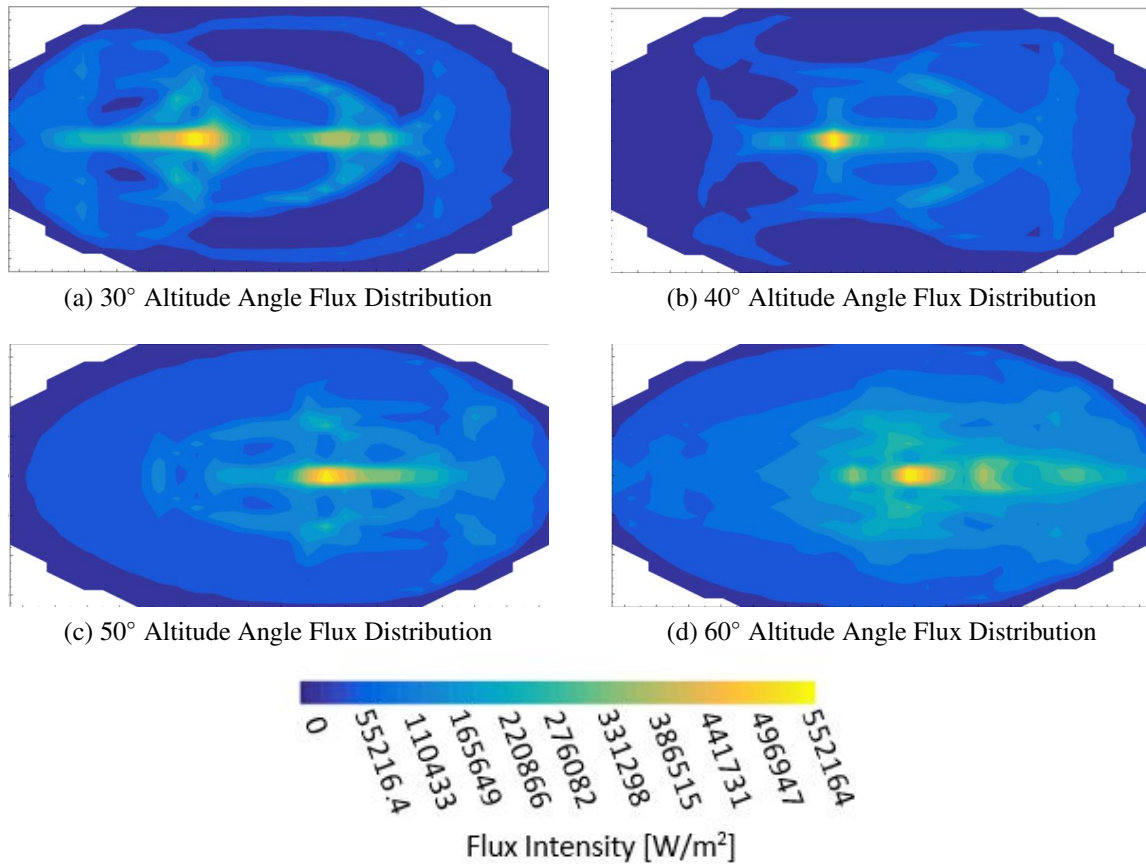
Figure 2.13: Flux distribution on optical conduit receiving surface for varying dish altitude angles

2.5.1   Numerical Comparisons and Discussion

As mentioned in Section 2.3.1, absorbed energy in this Gregorian system will be equal to the number of rays striking the surface and the energy per ray, thus should not vary between increasing ray counts. To examine this congruency a numerical comparison was conducted between the calculated absorbed power values simulated by Tracer™ and SolTrace™. Figure 2.14 depicts the power absorbed by incident rays on the bottom receiver surface computed by both programs at their respective ray count.
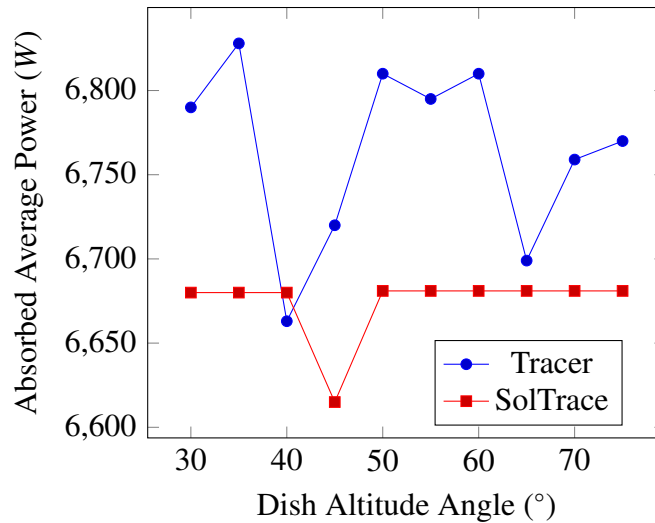
Figure 2.14: SolTrace and Tracer absorbed power for analogous configurations at varying dish altitude angles

While a ray count of 10,000 was chosen for Tracer[TM] (see Section 2.3.2), the appropriate ray count for the SolTrace[TM] model was 1,000,000. As depicted in Fig. 2.14, both absorbed powers are within a 5% range for both simulations despite SolTrace[TM] having 100 times more rays than that of Tracer[TM]. This is due to congruency in the optical design used in both programs as well as a consistent input flux equal to the solar constant. Tracer's[TM] open source python base adds greater flexibility to program conditions, but the underlying code has lower accuracy. Further advancements to Tracer's[TM] code must be done for the program to produce the consistent, accurate results depicted by the research tool developed by NREL, SolTrace[TM]. SolTrace[TM] is a more sophisticated program with better accuracy than Tracer[TM], capable of utilizing more computational power through usage of multiple processing cores along with a user-friendly interface developed for research. Thus, the results predicted by SolTrace[TM] are more consistent with variation in altitude angle for absorbed power in dimensionally congruent conduits.

Figure 2.15 is a graphical depiction of the results of average flux at the receiver surface in the bottom of the optical conduit, obtained for both programs. Again, the discrepancy in results between programs is seen. The results show that the discrepancy between the results from two programs is within 15%. SolTrace[TM] results show much more consistency between results of altering altitude angle. SolTrace[TM] also provides mapped heat flux distribution at a much higher resolution due to its immense ray count capabilities, as seen below in Fig. 2.16.
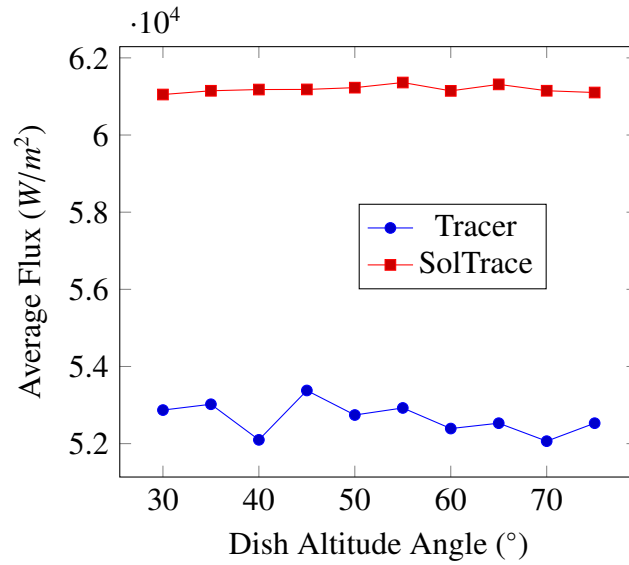
Figure 2.15: SolTrace and Tracer average absorbed flux generated in optical conduit

(a) SolTrace 45° Flux Distribution

(b) Tracer 45° Flux Distribution
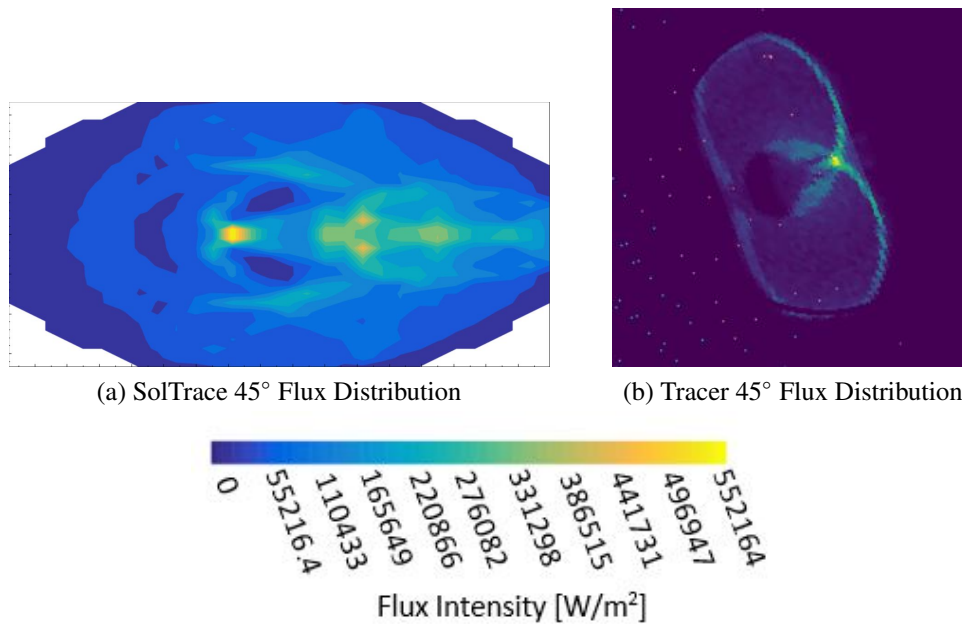
Figure 2.16: Flux distribution developed at bottom of optical conduit for SolTrace[TM] and Tracer[TM] at a 45° altitude angle and analogous configurations

Though the predicted contours are similar, with a local concentration near the centre and a somewhat parabolic concentration surrounding it, Fig. 2.16a (SolTrace[TM]) shows better distribution with higher detail than that of Fig. 2.16b (Tracer[TM]). The above depictions of flux indicate the intensity of radiative energy that will be absorbed into the receiver surface. Areas of higher concentration will generate higher temperatures in the receiver surface; a trait that may not be desirable despite its high heat transport rates due to its destructive capabilities of

material. Low areas of concentration pose no threat to material integrity, but possess lower rates of radiative heat transfer. Modelling techniques that are able to predict flux distribution intensity, such as the methods mentioned above, are integral tools in the progression of solar thermal energy as they can indicate designs for optimal charge processes of latent heat storage. Using SolTrace™'s vividly mapped heat flux distributions the radiative heat transfer into the PCM can be calculated with confidence. The practical limit of rays produced by SolTrace™ can also be attributed to the utilization of multiple processing cores, strengthening the computational power of the program.

The above results clearly indicated SolTrace™ as the superior ray trace program for use in further work developing the optical guide and Gregorian dish system. Further development and testing must be conducted on Tracer™ in order for it to achieve the same reliability and functionality to that of SolTrace™.

Chapter 3

Thermal Storage Integration for Water Heating Application

Design of the Gregorian parabolic dish solar collector is ultimately to store the heat in a thermal storage for utilization in a solar water heating system (see Fig. 1.6). The proposed system comprised of a shell and tube heat exchanger, where the shell side (filled with PCM) serves as the thermal energy storage and the water circulating through the tube side, caries the heat from the thermal storage to a hot water tank, which provides a hot water load for a given application. The optical guide designed in the previous chapter provides the high-quality thermal energy, which is used to charge the thermal storage unit, but further analysis is required for accurate sizing of water heating components to transfer energy from the thermal storage to the water heating load.

This chapter focuses on the development of the framework of a thermal energy model to characterize the thermal energy transfer from the parabolic dish concentrated solar energy system, to the thermal energy storage as well as the transfer of heat from the storage to the water heating load. A detailed parametric analysis was also conducted to investigate the influence of various key parameters on the system performance, which is vital for the design considerations of this coupled system in practical applications.

3.1 Mathematical Models

An accurate parametric evaluation of the proposed thermal storage unit for the water heater requires several assumptions and mathematical models. The proposed heat exchange design incorporates a commonly used shell and tube configuration in which the phase change material (PCM) i.e. thermal energy storage surrounds tubes which carries the heat transfer fluid (HTF) [76, 77, 78].Volume for the shell of the heat exchanger containing the PCM as well as the heat transfer surface area required by the tube(s) which could be computed based on residential or industrial heating needs. Charge and discharge of the thermal storage system is highly dependent on solar collector's surface area, rendering it an integral design consideration. In the present study, the heat transfer rate required for domestic hot water needs is used to determine the total required surface area for the solar collector. The theoretical closed loop heat exchange system that will be considered is depicted in Fig.3.1.

(a) Shell and Tube Configuration   (b) Singular Unit Schematic
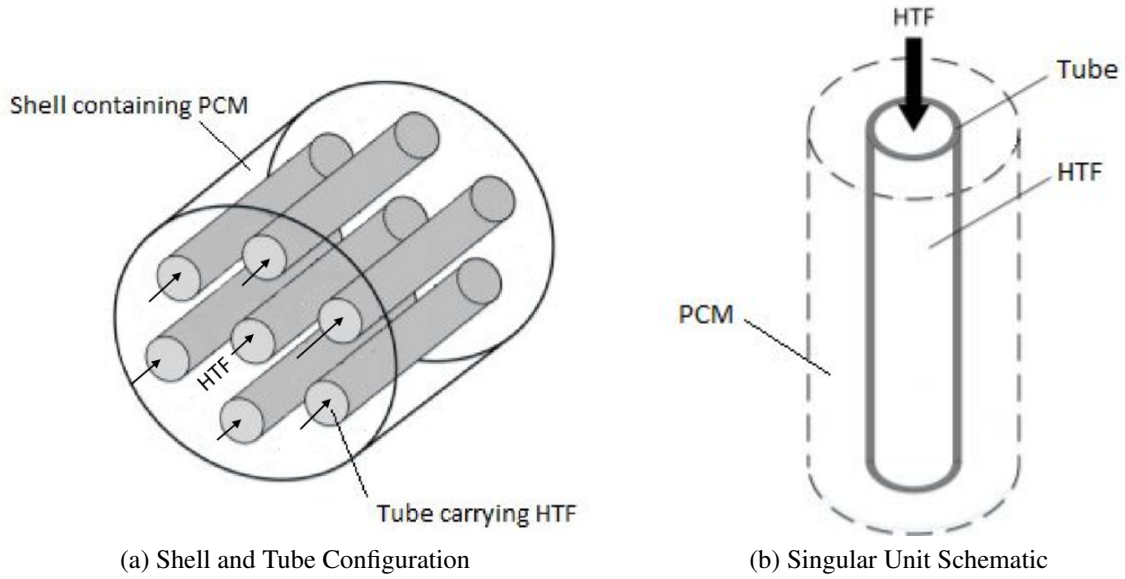
Figure 3.1: Proposed shell and tube heat exchanger with PCM for thermal storage (complete configuration and single element) [78]

3.1.1 Concentrated Solar Collector

A theoretical heat transfer rate for any solar collector, Q_{sc}, can be calculated through Eq. 3.1 [12].

$$
\begin{aligned}
Q_{sc} &= I_{sc}A_{sc}\eta_{sc} \\
&= I_{sc}(A_{ap} - A_{sh})\eta_{sc}
\end{aligned}
\tag{3.1}
$$

Overall thermal efficiency of the system, η_{sc}, is found through experimental study [79]; while incident solar radiation, I_{sc}, varies with time of year and location of the collector and is readily available through online databases. A colormap of the measured average global solar irradiance distribution is shown in Fig.3.2. Total collector area, A_{sc}, is equal to the aperture area of the collector, A_{ap}, with exclusion of the area of collector that is shaded by the receiver, A_{sh}. Equation 3.1 is useful for theoretical area approximations for collectors with a known heat transfer duty as insolation and efficiency can be estimated through literature and depicts the dependence of solar collector sizing on solar intensity .
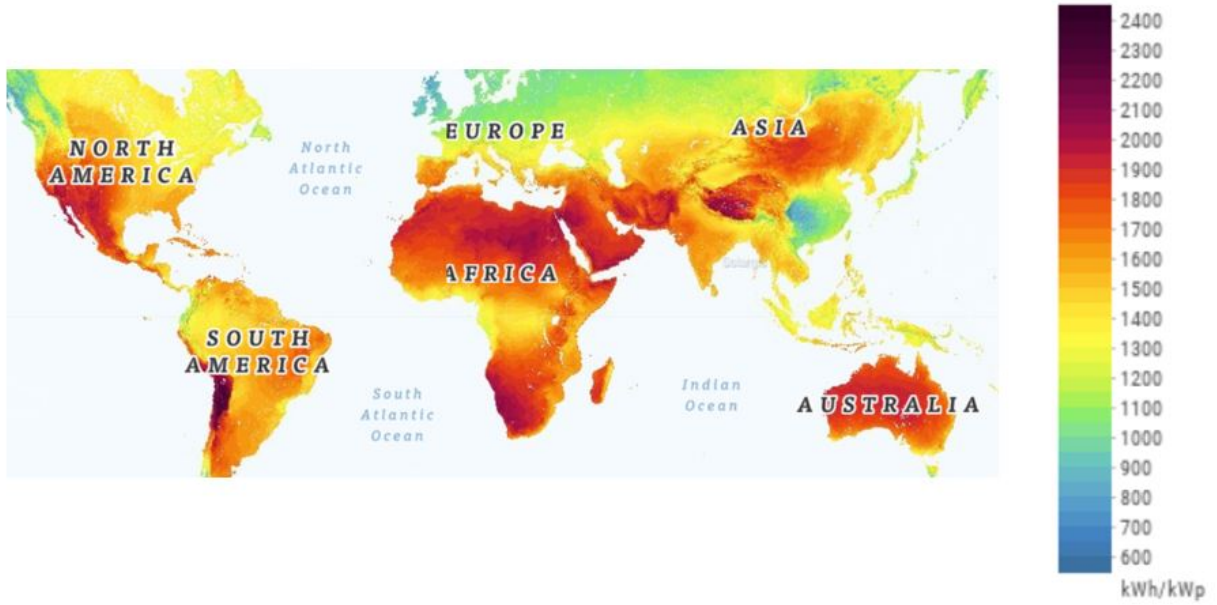
Figure 3.2: Measured average global solar irradiance distribution [80]

3.1.2   Phase Change Material (Thermal Storage Medium)

Determination of phase change material volume is based on an estimate of the heating needs for domestic hot water supply and latent energy storage capacity of specific phase change materials. The system must be able to fully charge the thermal storage unit within an amount of time specified by the hours of available daily insolation, thus daily available time to charge the thermal storage unit is also an important consideration in dictating PCM size. The total heat transfer needed for a residential hot water load, Q_w, can be estimated as [69]:

$$Q_w = m_w C_{p,w}(T_{o,w} - T_{i,w}) \tag{3.2}$$

where m_w represents required mass of hot water to be supplied for domestic usage, the specific heat of water is denoted by $C_{p,w}$ and $T_{o,w}$ and $T_{i,w}$ represent estimates of the outlet and inlet supply water temperatures, respectively.

The mass and volume of phase change material required is determined by the total energy storage capacity of the system. The total amount of thermal energy stored, Q_{PCM}, can be obtained through [81]:

$$\begin{aligned}
Q_{PCM} &= m_{PCM}(C_{p,s}\Delta T_s + L_f + C_{p,l}\Delta T_l) \\
&= m_{PCM}(C_{p,s}(T_{i,s} - T_m) + L_f + C_{p,l}(T_m - T_{f,l}))
\end{aligned} \tag{3.3}$$

Equation 3.3 defines total heat storage capacity of a PCM as a sum of the sensible heat generation in each of solid and liquid phases, as well as the latent heat through solid-liquid phase transition. Latent heat of fusion, L_f, is constant for both melting and solidification processes; while the specific heats for solid and liquid phases, $C_{p,s}$ and $C_{p,l}$ respectively, are different. The temperature difference at solid state, ΔT_s, is determined by operating conditions of the heat exchanger. Operating temperatures of typical solar water heaters, $T_{i,s}$, begin storage of useful energy for solid to liquid transition at approximately 30°C, providing it is below the melting temperature of the material, T_m [76]. Operating ranges exist mainly due to hot water temperatures below 30°C not being suitable for domestic applications, thus energy need not be drawn from the water heating system for usage at those temperatures. Once the material has been through the complete melting process, it can further store sensible heat through sensible heating (in the liquid state) until a final liquid temperature, $T_{f,l}$ is reached.

The phase change material volume, V_{PCM}, is the associated volume needed for required heat transfer, Q_{PCM}, based on the phase change material mass, m_{PCM}.

$$V_{PCM} = \frac{m_{PCM}}{\rho_{PCM,l}} \tag{3.4}$$

Volumetric expansion is accounted for in Eq. 3.4 through the use of phase change material's liquid density, $\rho_{PCM,l}$. Use of liquid density ensures maximum theoretical volume, but experimental testing is required for the most accurate expansion factors and to be certain that the thermal storage unit can accommodate the volume changes [82].

3.1.3 Heat Exchanger

The transfer of heat from the thermal storage to the hot water load is via heat exchanger tube embedded inside the thermal storage unit (i.e. the tube side of the shell and tube heat exchanger). This heat exchanger is used to increase the temperature of water supplied at the typical residential water supply temperature to a temperature that is required for the utilization of domestic hot water (see Fig. 3.3). Heat transfer in the tube side of the exchanger is governed by internal forced convection, and the thermal resistances associated with it are shown in Fig. 3.3. Several assumptions are made in order to simplify the mathematical model used to size the heat exchanger, beginning with the assumption of internal laminar flow within the tube. Due to latent heat storage operating mainly at the melting temperature of the PCM, the heat transfer tubes are assumed to be subjected to a tube wall temperature near identical to that of PCM melting temperature. Assuming that over long operation periods the main mechanism of heat transfer occurs under a constant tube wall temperature, the resulting correlation for the Nusselt number, Nu, is: [83].

$$Nu = \frac{h_i D_h}{k_w} = 3.66 \tag{3.5}$$

Under the laminar flow constant wall temperature assumption; the internal natural convection coefficient, h_i, is constant for a given hydraulic diameter, D_h and water thermal conductivity, k_w. Reynolds number for the associated laminar flow within a pipe is equal to or less than 2100.

Overall heat transfer between the tube and encasing phase change shell is estimated under the assumption of convection being the sole heat transfer mechanism outside of the HTF tube (see Fig. 3.3). This eliminates complications that arise when trying to incorporate the amount of time that the PCM is solidified, introducing conductive heat transfer outside the tube, while remaining fairly accurate as the majority of operation will be conducted under convective conditions.
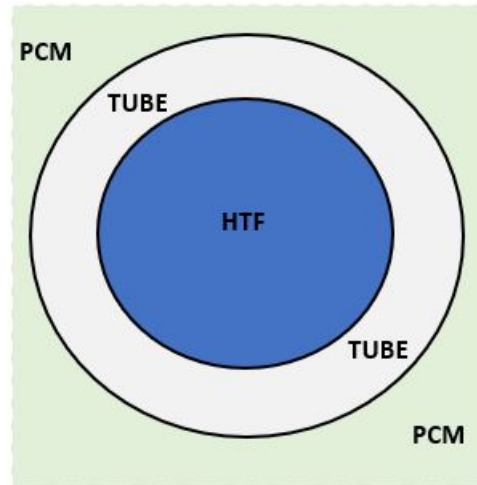
(a) Cross Sectional Schematic of Single
Shell and Tube Element
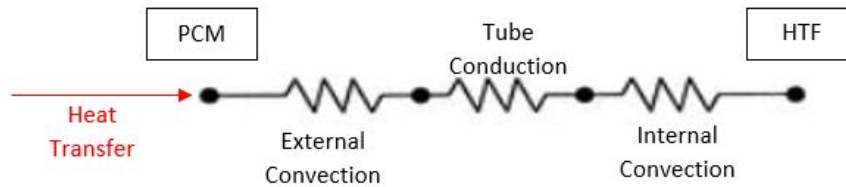
(b) Equivalent Thermal Resistance Circuit

Figure 3.3: Shell and tube heat exchanger cross sectional schematic and resistance circuit diagram

The corresponding overall heat transfer coefficient, U, can be found using Eq. 3.6 with determination of the outer convective heat transfer coefficient, h_o [83].

$$\frac{1}{U} = \frac{r_o}{r_i h_i} + \frac{r_o}{k} ln(\frac{r_o}{r_i}) + \frac{1}{h_o} \tag{3.6}$$

Equation 3.6 denotes r as radius of the tube, with subscripts o and i representing the tube's outer and inner surface respectively.

The rate of heat transfer required to supply a domestic hot water heater, $\dot{Q}_w$ can be computed with the use of Eq. 3.2 and determination of an appropriate 'Exposure Time', t, for the solar

water heating system.

$$\dot{Q}_w = \frac{Q_w}{t} = \dot{m}_w C_{p,w}(T_{o,w} - T_{i,w})$$ (3.7)

Mass flow rate of water through the collector is represented by $\dot{m}_w$ in Eq. 3.7. The exposure time, t, defines the amount of time in seconds for the circulating water to be heated from $T_{i,w}$ to $T_{o,w}$ at the heat transfer rate $\dot{Q}_w$. The solar collector is required to accommodate the amount of energy required for daily domestic hot water requirements, while the heat exchanger must accommodate and transfer heat at a rate sufficient for use; thus exposure time essentially dictates sizing for both of these systems.

Due to the assumptions on the shell side of this heat exchanger configuration, only phase change occurs as a heat transfer mechanism to the tube. This allows the comparison to be drawn between this heat exchanger and that of a condenser or evaporator under similar conditions[84]. Under this assumption, the overall thermal resistance, R_{tot} can be calculated by Eq. 3.8 [83, 84].

$$R_{tot} = \frac{1}{UA_{hx}} = -\frac{1}{\dot{m}_w C_{p,w} ln(\Delta T_o / \Delta T_i)}$$ (3.8)

$$\Delta T_o = T_m - T_{o,w}$$

$$\Delta T_i = T_m - T_{i,w}$$

The overall heat transfer surface area is represented by A_{hx} and mean temperature differences for outlet and inlet tube conditions are denoted by ΔT_o and ΔT_i respectively. The outer wall tube surface is assumed to be at the PCM melting temperature, thus T_m is the driving factor for inlet and outlet mean temperature differences.

A theoretical energy model using these equations is implemented in Excel^{TM}.

3.2 Operating Conditions

The solar water heating system will operate at known conditions of insolation and inlet and outlet water temperatures. Domestic hot water usage is relative consistent throughout North America and is dependent on household occupants. Based on ASHRAE estimations, volumetric ranges for an occupancy of 2, 3 and 4 people are 167L, 212L and 257L, respectively [85]. Incident solar irradiation varies dependent on distance from the equator, thus different countries experience different intensities of solar energy. Canadian data banks containing measurements of global horizontal and direct normal irradiance is used for approximations; with peak average values of insolation ranging from approximately $600W/m^2$ in central Alberta, to $500W/m^2$ in Toronto [86].

Residential water loads have been studied for volumetric usage as well as inlet and outlet temperature conditions. Domestic hot water is typically supplied at an average temperature of 60°C; while cold water inlet temperatures are dependent on the month of the year, with summer water temperatures near 16°C and winter temperatures of approximately 9°C [87]. This is crucial in sizing of thermal storage volume and heat exchange system, as a greater rate

of energy transfer will be needed for months with lower inlet temperatures, and vice-versa. For realistic sizing of the solar water heating system, the phase change material and heat exchanger should accurately reflect this seasonal variation of supply water temperatures.

3.3   Parametric Study

To analyse the impact that various operating conditions have on the sizing of the proposed solar water heating system, a parametric study is conducted using the developed energy model. This parametric study will provide the framework for sizing methodologies for the proposed solar collector system as well as the latent heat storage unit. A variable exposure time dictates the number of hours, that the solar collector will be subjected to insolation. Exposure time is analogous to the number of hours in a day that can be utilized for charging the heat storage and is heavily determined by geographical location due to Earth's rotation and tilt. Once an exposure time is determined, the required supply load of domestic hot water can be used to determined the size of solar collector. The process to computing solar collector and thermal storage sizing is depicted in Fig. 3.4.
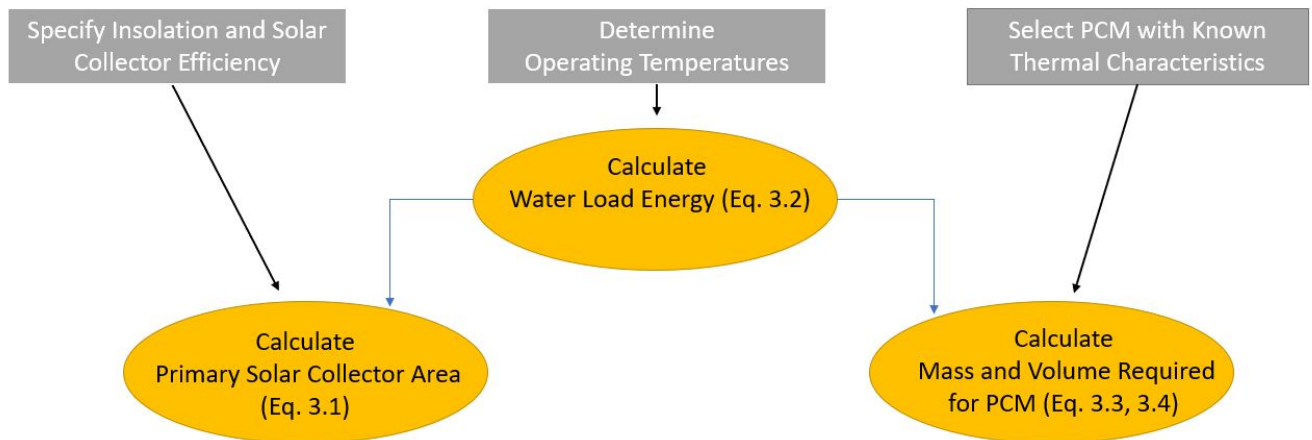
Figure 3.4: Flow chart determining area of solar collector and mass and volume of PCM for solar water heating at a specified load and operating temperatures

Energy required to supply the water load is computed through the use of Eq. 3.2 and determination of a suitable supply water volume. In a fully ideal heat transfer process, all energy transferred to the water would be directly from the thermal energy storage discharge process. This leads to the assumption of equating the energy required to fully supply hot water at some operating temperature to the energy stored in the PCM. Mass of the PCM is determined through rearrangement of Eq. 3.3 and a selection of heat storage operating conditions. Volume of the thermal storage is calculated through use of Eq.3.4 and the density of the liquid PCM. Solar collector area is proportional to the amount of energy required for the usage, thus can be calculated based on the rate of energy it is required for heating water for domestic usage over the exposure time (see Eq. 3.7). Required parameters used as a testing baseline for the solar

collector and thermal storage were determined through literature study and can be found below in Table 3.1. Sample calculations at an exposure time of 6h for determining solar collector area and thermal storage volume and mass for a 70L water load can be found in Appendix D1.

Table 3.1: Default test conditions for preliminary parametric study and sample calculations of solar collector and PCM based on literature survey

Variable	Value	Description	Used in Eq.
I_{sc} $[W/m^2]$	288.71	Solar Intensity for Toronto, Ontario for the Month of September	3.1
η_{sc}	0.75	Solar Collector Efficiency	3.1
ρ_w $[kg/m^3]$	997	Average Inlet Water Supply Density	3.2
$C_{p,w}$ $[kJ/kgK]$	4.178	Specific Heat Capacity of Water	3.2
$T_{i,w}$ $[°C]$	12	Inlet Water Supply Temperature: Monthly North American Average	3.2
$T_{o,w}$ $[°C]$	60	Average Outlet Temperature Domestic Hot Water	3.2
$T_{i,s}$ $[°C]$	57.2	Initial Operating Temperature of PCM at Solid State	3.3
T_m $[°C]$	72.2	Melting Temperature of Selected Phase Change Material	3.3
$T_{f,l}$ $[°C]$	87.2	Final Temperature of Liquid State PCM	3.3
$C_{p,s}$ $[kJ/kgK]$	2.4	Specific Heat Capacity of Selected PCM at Solid State	3.3
L_f $[kJ/kg]$	267	Latent Heat of Fusion of Selected PCM	3.3
$C_{p,l}$ $[kJ/kgK]$	4.57	Specific Heat Capacity of Selected PCM at Liquid State	3.3
ρ_l $[kg/m^3]$	1280	Density of Selected PCM at Liquid State	3.3

As a test case, solar irradiance is measured for Toronto, Ontario during September. September has values of solar irradiance that closely match the average yearly value, thus can be used to estimate model sizing for the majority of Summer and Spring months. Initial and final supply water temperatures are determined from the literature, along with phase change material characteristics. The default phase change material considered is $Na_2SiO_3 5H_2O$, with readily available thermophysical properties [88]. Operating range for the solid and liquid material states are $\pm15°C$ above and below the melting temperature of the selected phase change material, T_m. Operating ranges are chosen which are suitable for residential water heating. A solar collector efficiency of 75% was estimated to account for potential losses in a realistic system, specifically at the thermal interface between the surface of component D and the PCM, which is not analysed in this study.

Calculation of the overall heat exchanger surface area for the proposed design requires use of shell and tube heat exchanger equations and specific assumptions. The framework presented will allow for calculations of suitable sizing of heat exchanger for domestic usage. Internal convection of the heat exchanger is considered to be governed by laminar flow conditions in the tubes, while conductive heat transfer is dictated by the tubes' thickness and material

selection. The main mechanism for external thermal resistances is assumed to be the convection associated with the phase change material during phase transition outside of the tube. This is due to the PCM being in phase transition for the majority of its operation and thus at a constant temperature. Under these assumptions, correlations for Nusselt number and a constant temperature tube wall with laminar internal flow can be used to estimate the proposed internal convection heat transfer coefficient. Heat exchanger design literature suggests a tube subjected to only phase change in the shell will yield a total thermal resistance equal to that of Eq. 3.8; thus, the procedure to calculate heat exchange surface area is presented in Fig. 3.5.
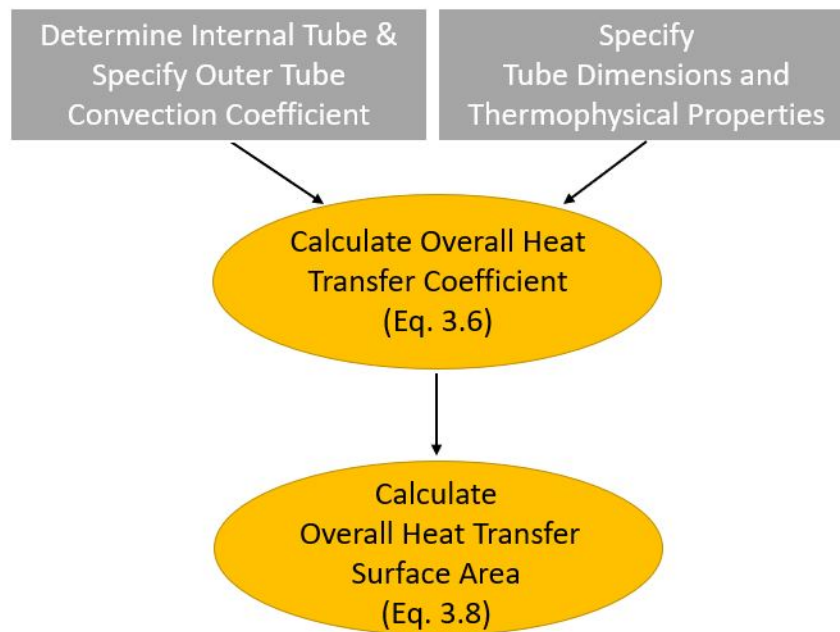
Figure 3.5: Flow chart to compute overall heat exchanger surface area on the tube side of proposed heat exchanger

Once mass flow has been computed (see Eq. 3.7), the overall thermal resistance can be computed with the operating conditions mentioned in Table 3.1. To conduct further analysis on the effects of internal convection, external convection and tube conductivity on overall size of the heat exchanger a set of default parameters in Table 3.2 will be used.

Table 3.2: Default tube conditions for preliminary tests on heat exchanger surface area

Variable	Value	Description	Used in Equation
t [m]	0.002	Tube Thickness	-
Nu	3.66	Nusselt Number at Operating Conditions	3.5
h_o [W/m^2K]	1800	External Tube Convection Coefficient	3.6
h_i [W/m^2K]	186	Internal Tube Convection Coefficient	3.6
k_w [W/mK]	0.613	Water Conductivity	3.6
k [W/mK]	205	Tube Conductivity	3.6
r_o [m]	0.006	Tube Outer Radius	3.6
r_i [m]	0.008	Tube Inner Radius	3.6
ΔT_o [$°C$]	12.2	Temperature Difference Tube Outlet	3.8
ΔT_i [$°C$]	60.2	Temperature Difference Tube Inlet	3.8

Sample calculations for determining the overall heat exchanger area can be found in Appendix E1. Material conductivity was chosen to be that of Aluminium for test conditions, with outer tube convective heat transfer coefficient approximated from literature for phase change materials under analogous conditions in the shell side of a heat exchanger [89].

3.3.1   Effects of Water Supply Load and Exposure Time

The effect of water supply on the sizing of solar parabolic dish concentrator surface area and heat exchanger area is examined by altering exposure time at varying water loads. This correlation depicts the estimated size of solar collector required to supply domestic hot water for a house hold of 1 - 5 people assuming each person uses 70L of hot water a day. Size requirements of the solar collector determine the feasibility of its application as requirements for water loads in specific regions and daylight hours may be vastly different. Large solar collector areas can theoretically be divided into several dishes of a desired diameter for domestic integration. Figure 3.6 depicts the relationship between supply water and solar collector area for Toronto, Ontario during the month of September under default operating conditions described in Tables 3.1 and 3.2.

The relationship in Fig.3.6 between hot water supply load and solar collector area depicts a strong correlation between solar collector area and exposure time. As expected, increasing the water load will result in a required increase of solar collector area for a constant daylight time; while a decrease in the size requirements for increasing exposure time is observed. Differences between exposure times of 10h and 12h are smaller than that of exposure times of 6h and 8h, depicting exposure time's weakening impact to solar collector area at higher magnitudes. This may be crucial in determining the location of the proposed solar water heater as sizing a dish for areas with longer daylight may not prove to be beneficial for collector required area when
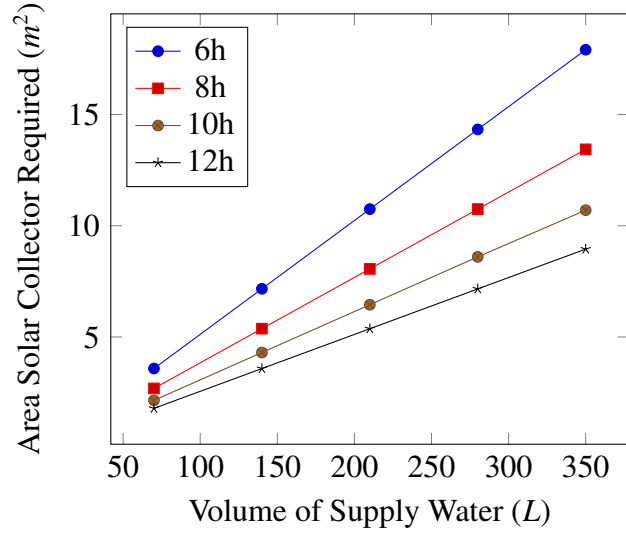
Figure 3.6: Required solar collector surface area versus the demand of domestic hot water at variable loads, for different daylight times

considering locations of higher exposure times. This correlation is further examined in Fig. 3.7 where the overall heat exchanger area for cases identical to that above at default conditions are represented. Overall heat exchanger area is defined as the required surface area for sufficient heat transfer to occur between the heat exchanger and the domestic water supply.
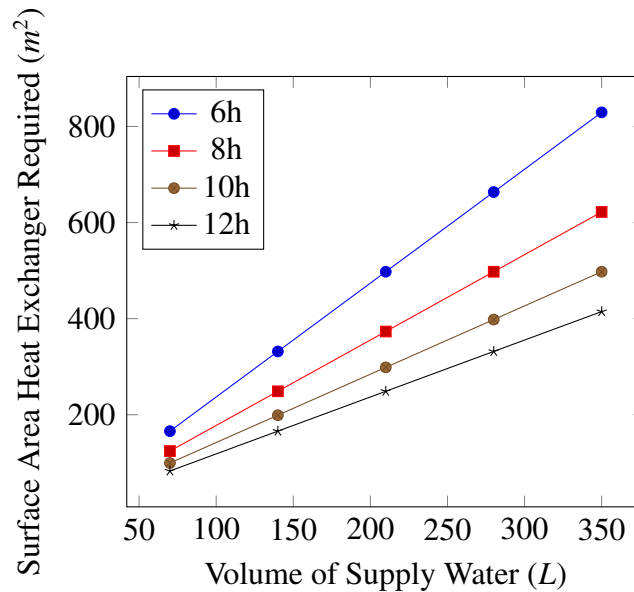

Figure 3.7: Required heat exchanger surface area to supply domestic hot water at variable loads and daylight times

Similar conclusions can be drawn for the area of heat exchanger as the relationship depicted between supply water, varying exposure time and required overall surface area is analogous to

that of the solar collector. For larger water loads, the influence of decreasing daylight time has a larger impact than the area required at lesser supply loads. The area required for total heat exchange at maximum load of 350L and a 6h exposure time is 33% larger than that of the area required for 8h exposure time at analogous conditions; while the difference in area between 8h and 10h is only 25%. This effect increases in proportion to exposure time as increasing from 10h to 12h only reduced area by 20%. Though an increase in daylight hours show a significant decrease in required surface area, these values are relatively large for domestic usage; thus the conducted study should be used as a framework for future design methodology of solar water heating systems, rather than development of a real system.

3.3.2 Global Position

Incident solar radiation varies globally (see Fig. 3.2) thus location of this solar water heating system also dictates its size. For a preliminary test, analogous systems in Red Deer, Alberta and Toronto, Ontario are compared under default conditions for varying water loads and exposure times to depict the effect of a variation of solar insolation. The results depicted for Red Deer are also be under the same default conditions mentioned in Table 3.1 and Table 3.2 with the exception of I_{sc} being equal to 371.24 W/m^2; the insolation at that location based on Canadian national databases, instead of the insolation in Toronto of 288.71 W/m^2.
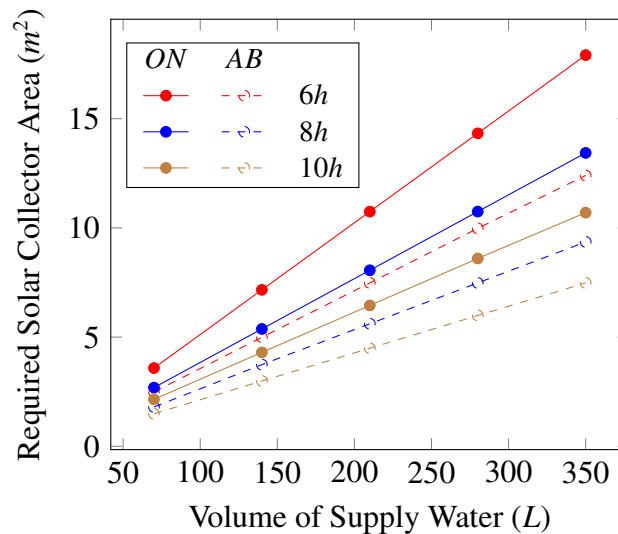
Figure 3.8: Required area of solar collector for Toronto and Red Deer under analogous conditions and varying exposure time and water loads

Since mass flow rate is proportional to exposure time and not intensity of solar radiation, the insolation does not affect required heat exchange area and only influences overall solar collector area. Each location has greater variation in solar collector area for lower exposure times, with differences of about 33% and 25% decrease in surface area between 6h to 8h and 8h to 10h. Further analysis of Fig. 3.8 shows the significant influence of insolation on required solar collector area. At a max load of 350L and minimum exposure time of 6h, the solar

collector in Red Deer would require approximately 44% less area than the solar collector in Toronto. Insolation in Red Deer is only 29% greater than that of Toronto, yet results depict a greater influence on required surface area for these conditions. These results are consistent with exposure times and highlight the reliance of a suitable location for the success of solar water heaters. Analysis of the above data indicates the advantages of the solar water heater in areas with long day-light hours and high incident solar radiation for optimal performance.

3.3.3 Influence of PCM Selection

Thermophysical properties of phase change materials substantially influence sizing requirements for the shell side heat exchange system. Energy density of PCMs vary with composition, thus a comparison of two materials with properties available through literature is conducted to determine the most favourable characteristics for the proposed solar water heating system. Commercial PCMS comparable to the default PCM ($Na_2SiO_35H_2O$) are selected based on latent heat of fusion and melting temperatures. The properties of these PCMs are listed in Table 3.3.

Table 3.3: Thermophysical properties of commercially available PCMs [90]

PCM	$C_{p,s}$ [kJ/kgK]	$C_{p,l}$ [kJ/kgK]	ρ_l [kg/m^3]	L_f [kJ/kg]	T_m [$°C$]
$Na_2SiO_35H_2O$	2.4	4.57	1280	267	72.2
0500- Q65 BioPCM	3.5	3.4	1050	225	65
0500- Q93 BioPCM	3.5	3.4	1050	220	93

The above PCMs have a lower latent heat than the default selection, but higher melting temperatures. Results for alteration of phase change material under otherwise default conditions, at an exposure time of 6h are depicted below in Fig. 3.9.
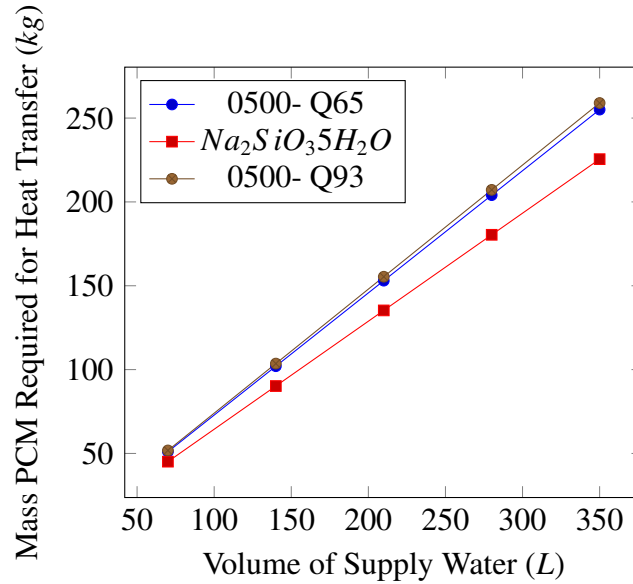
Figure 3.9: Required mass of PCM to supply domestic hot water at variable loads at an exposure time of 6h

For analogous operating conditions, Fig. 3.9 illustrates a weaker discrepancy in mass of the phase change material between lesser loads of water than that of greater; but a correlation between melting temperature of the phase change material and its required mass of even less significance. The default phase change material would pose a reduced mass of over 14% at a supply water of 350L during a 6h exposure time, while the difference in mass is less than 1% towards a water load of 70L. Q65 and Q93 show negligible variation in required mass despite their vast melting temperature differences; likely a result of their similar latent heats of fusion and densities. Results indicate mass of $Na_2SiO_35H_2O$, and thus the spatial requirements of the latent thermal storage system, are reduced compared to other options due to its higher latent heat storage capability. These results further encourage the use of storage materials with high latent heat capacities. The default phase change material also possesses a higher liquid density than its counterparts, further increasing sizing differences when considering volume. Based on results in the above section it is also reasonable to assume that at exposure times greater than the tested 6h, the performance of the solar water heater containing $Na_2SiO_35H_2O$ would only increase comparatively.

Figure 3.10 depicts a smaller overall heat exchanger area for Q93 compared to its counterparts. This is a result of the assumption made in calculating thermal resistance associated with the heat exchange tube being the outer wall of the tube is equal to that of the melting temperature of phase change material. Due to the extremely high melting temperature of Q93, the outer wall of the tube is maintained at a higher temperature; thus mean inlet and outlet temperatures are increased, resulting in a higher thermal resistance and lower overall required area (see Eq. 3.8). A 77% reduction in heat exchange area is consistently observed for varying water loads between default phase change material and Q93. This is contradicting to the results depicted in the mass and volume of phase change material required; indicating a steep trade-off between overall heat exchange area and the required mass of PCM.
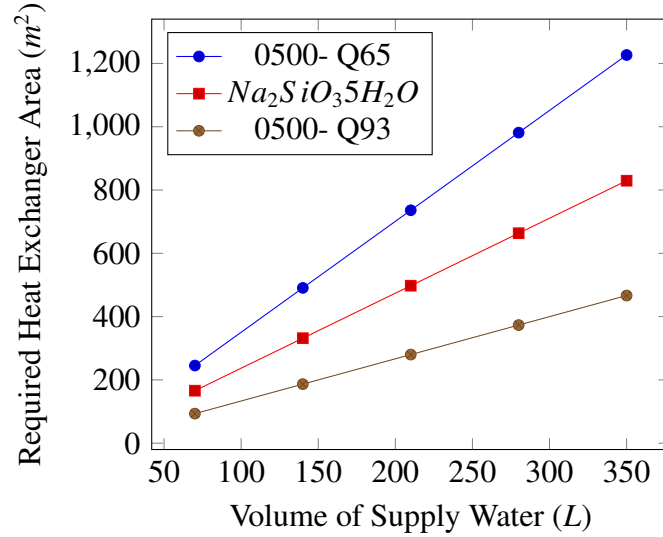
Figure 3.10: Required area of heat exchanger for different material selections of PCM to supply domestic hot water at variable loads at an exposure time of 6h

3.3.4   Internal Heat Transfer

Tube thermal conductivity effects the sizing requirements. Heat exchange surface area as materials of higher conductance require less heat transfer area to provide the same outlet temperatures. A large, thick tube will have a stronger mechanism of conductive heat transfer, making it necessary to examine effects of its associated thermal resistance to optimize sizing of the solar water heater. The influence of this parameter is examined at an exposure time of 6h under default conditions, listed in Tables 3.1 and 3.2, for various thermal conductivities.

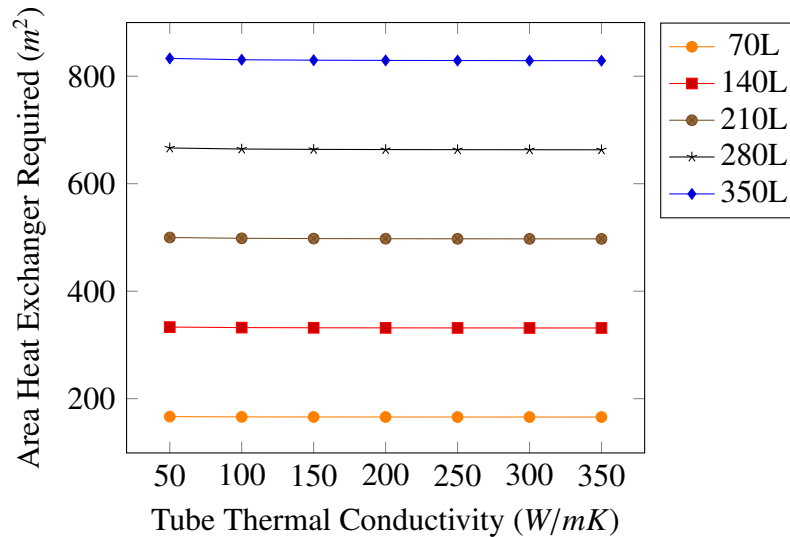

Figure 3.11: Required heat exchanger total surface area to supply domestic hot water at variable loads under varying tube conductivity for 6h exposure time

Equation 3.6 and Fig.3.11 illustrate the effect of thermal conductivity on the heat transfer surface area for different water load conditions. Relationship between tube conductivity and heat exchanger area is negligible compared to that of previously mentioned parameters. A variation of surface area less than 1% between thermal conductivity of $50W/mK$ and $350W/mK$ is seen consistently for each water load. The above results are likely due to the small size of tube dimensioned for default conditions, mentioned in Tables 3.1 and 3.2. Small tube diameter and thickness result in values of conductive thermal resistance lesser than that of larger dimensions; thus the tube conductivity has a negligible impact on sizing across water loads. Correlations suggest significantly increasing the tube thermal conductivity will yield heat transfer improvements of little to no value.

Spatial requirements limit the sizing of tube that can be utilized in solar water heaters. Variation of tube diameter results in a variation of internal convection heat transfer coefficient (see Eqn.3.5). Variation in tube diameter influences total thermal resistance and may determine whether or not a heat exchange system will require additional structuring, such as baffles to adjust for flow speed. Figure 3.12 illustrates the relationship between inner tube radius and the required heat exchange surface area for varying water loads at an exposure time of 6h under otherwise default conditions.
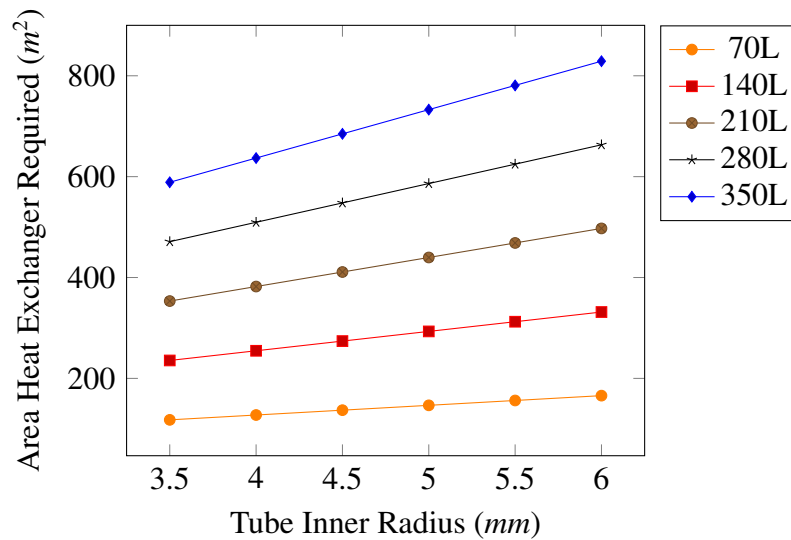
Figure 3.12: Required heat exchanger total surface area at variable loads under varying tube radius for 6h exposure time

As depicted above, variations of inner tube radius result significant alterations for heat exchange area for a specified water load. A consistent 71% reduction of heat exchange area for each individual water load is resulted from the decrease of inner tube radius from 6mm to 3.5mm. A minimal exposure time of 6h indicates that with increased time of insolation, these effects would be multiplied. Results are due to the significant affect diameter has on internal convection coefficient (see Eqn.3.5), and internal convections impact on overall heat transfer (see Eqn.3.6).

The effect of varying tube thickness was analysed under default conditions and a 6h exposure time. Tube thickness increases thermal resistances associated with internal heat transfer (see

Eqn. 3.6) thus, can significantly impact the sizing requirement of the heat exchanger. For the default case of inner tube radius of 6mm increasing tube thickness from 1mm to 3.5mm had a 33% increase on overall surface area across each water load. The results are depicted in Fig.3.13, which are similar to that of Fig. 3.12 and show that their impact on the sizing of solar water heater is more significant than that of tube thermal conductivity. Tube thickness plays a key role in the overall heat transfer mechanism between the tube and outer media as it increases the conductive thermal resistances to the heat transfer fluid, increasing the amount of energy required to bring the bulk fluid to operating temperature. Figure 3.13 depicts a max water load requiring a larger heat exchanger area for larger tube thickness increments than that of Fig. 3.12 for radius increments; leading to the suggestion of large tube thickness being more detrimental for optimal sizing of the proposed solar water heater than radius.
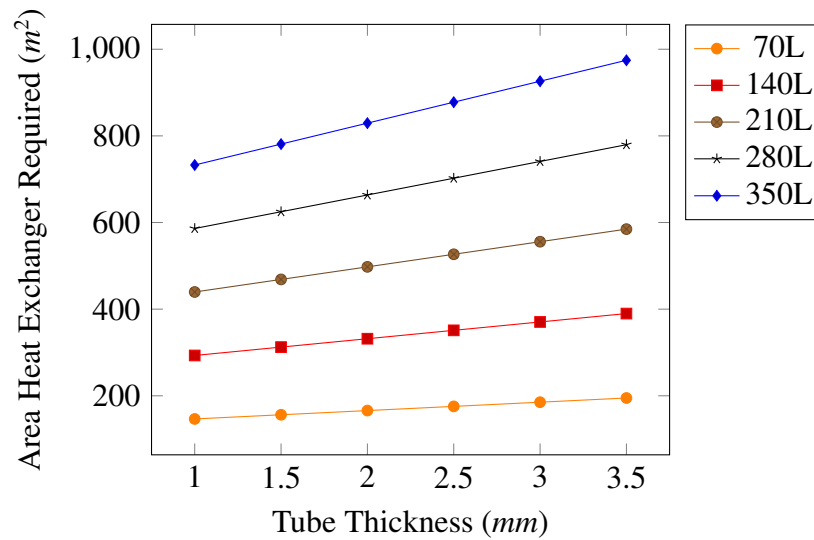
Figure 3.13: Required heat exchanger total surface area to supply domestic hot water at variable loads under varying tube thickness for 6h exposure time

Actual conductive heat transfer for this solar water heater can only be accurately depicted through experimental testing of phase change materials during their solid state and solidification processes. The data presented above is accurate for the framework of the proposed case, but will not reflect occurrence of the most realistic conductive heat transfer mechanisms due to a knowledge gap in behaviour of PCMs. Assumptions made provide an estimation of required sizing based on negligible conductance from the solid state PCM, thus actual required heat exchange surface area would be lower than that calculated above.

3.3.5   Overall Heat Transfer Coefficient

Approximation of the overall heat transfer coefficient as a default condition limited analysis in previous parametric studies. Although an accurate outer tube heat transfer coefficient has yet to be determined, its effects on required heat transfer surface area, is integral to the optimization of the proposed design. Based on a study conducted by Castell et al. [89], a reasonable range of

outer convective heat transfer coefficients can be determined for the natural convection mechanisms that occur within a PCM. Figure 3.14 depicts the relationship between overall required heat exchanger surface area and external tube heat transfer coefficient. Analysis was conducted at varying water loads for an exposure time of 6h under default conditions (see Tables 3.1 and 3.2).
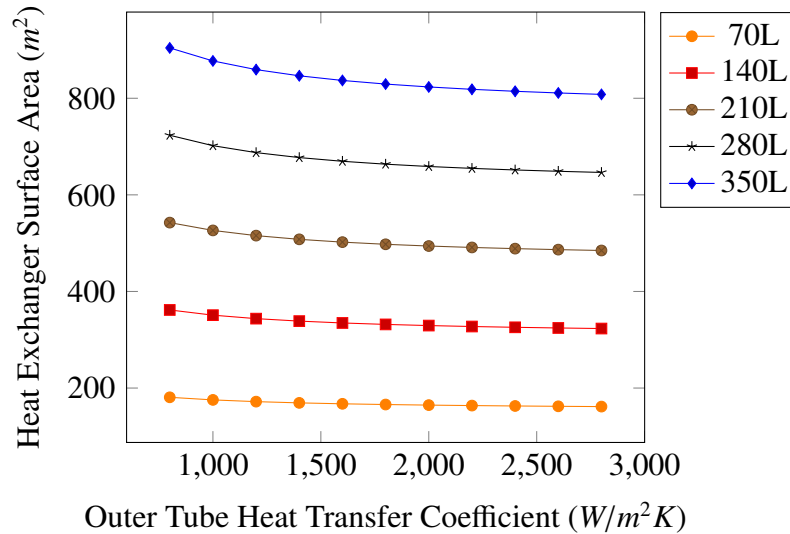

Figure 3.14: Heat transfer surface area to supply varying loads of domestic hot water under a range of outer tube convective heat transfer coefficients for 6h exposure time and default conditions

Increase of outer tube heat transfer coefficient from 800 to 2800 while keeping internal convection coefficient and tube conductivity constant resulted in a reduced area from 904.22 m^2 to 808.02 m^2 for the case of 350L. Results indicated a significantly lesser effect on the reduction of heat exchange surface for an increase of outer tube convection coefficient than increase of other parameters, such as exposure time (see Fig. 3.7). Having tests conducted at a load of 350L and 6h exposure time ensures maximum theoretical output. Due to this, an increase of exposure time, or decrease of water load would result in proportionally reduced sizing requirements than those presented above. The impact on sizing requirements from variation of outer heat transfer coefficient is largely due to its respective influence on the overall heat transfer coefficient. Results also depict a larger difference in heat exchange surface area for outer tube convection coefficients in the approximate range of 800 W/m^2K - 1,600 W/m^2K compared to 2,000 W/m^2K - 2,800 W/m^2K. Results in the later range test conditions (2,000 W/m^2K - 2,800 W/m^2K) differed by approximately 2% consistently for each water load; while the earlier ranges (800 W/m^2K - 1,600 W/m^2K) consistently produced discrepancies above 8%. This result indicates that sizing can be reduced through increase of outer tube heat transfer convective coefficient, but has limited paybacks when utilizing extremely high coefficients. Outer tube coefficient must be properly studied to present an accurate value of this parameter as PCMs have a complex melting process and a single value for the entire heat exchange process is only appropriate for the frame work of the proposed case.

Heat transfer surface area was parametrically studied and is depicted in Fig. 3.15 for varying internal and outer convective heat transfer coefficient. Tests were conducted for a water load of 350L and an exposure time of 6h under default conditions stated in Tables 3.1 and 3.2. Tests yielded similar results to that of Fig. 3.14 and depicted a sharp reduction in heat exchanger area with increase of inner tube convection coefficient in the earlier ranges; but depicted little to no. Variation of internal heat transfer coefficient from the range of $50W/m^2K$ to $150W/m^2K$ produced a reduction for heat exchanger required surface area of approximately three times its original size; while increase of h_i from $150W/m^2K$ to $350W/m^2K$ yield an area decrease of over 200%. Internal convection coefficient has the most significant impact on overall heat exchanger surface area when compared to every other examined parameter. This large influence is asymptotic at the later ranges, with a reduction of area between $300W/m^2K$ and $350W/m^2K$ of 15%. This minimal reduction in area when compared to the large variation at earlier ranges of internal convection coefficient depict little to no improvement of thermal performance with significant increase of internal tube convection coefficient. Similar to Fig. 3.14 varying the outer tube convective heat coefficient shows little correlation for tube required surface area for a water load. Table 3.4 lists the negligible changes in area between increments of outer tube convective coefficient. The results indicate that internal heat transfer mechanisms have the largest impact on heat exchanger surface area, thus variation of Nusselt number can obtain a suitable parameter for operation. . Once a thresh hold is met further increasing the magnitude of internal heat transfer coefficients would prove to have very little influence on overall heat exchanger surface area; but provide significant reduction in area for increments in lower ranges.
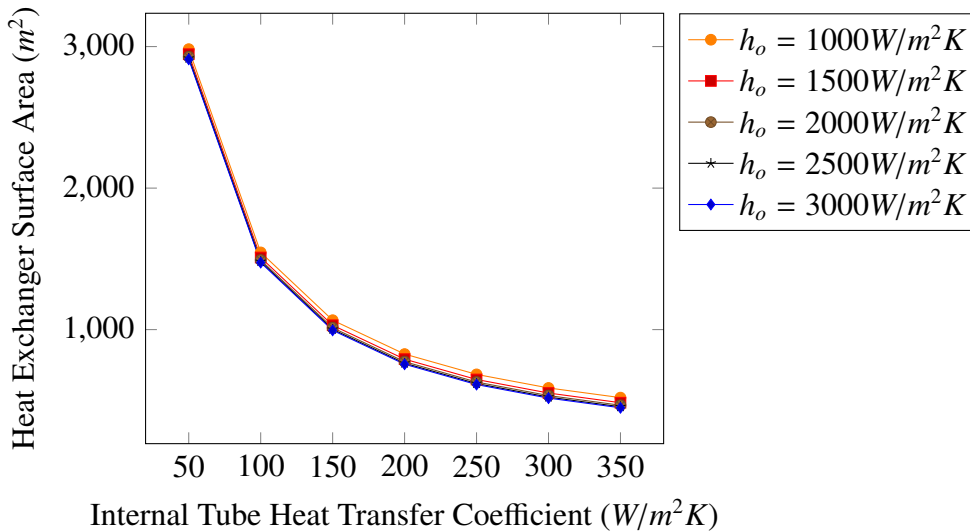

Figure 3.15: Heat transfer surface area to supply 350L domestic hot water under varying outer tube convective heat transfer coefficients and varying inner tube convective heat transfer coefficients for 6h exposure time

Table 3.4: Required heat exchange surface area based on varying inner and outer convection coefficients for default parameters. At 6h exposure time and 350L water load requirement

$h_i(W/m^2K)$	$h_o(W/m^2K)$				
	1000	1500	2000	2500	3000
	Required Surface Area (m²)				
50	2982	2946	2928	2917	2910
100	1545	1509	1491	1481	1473
150	1066	1031	1013	1002	995
200	827	791	773	762	755
250	683	647	629	619	611
300	588	552	534	523	516
350	519	483	465	454	447

3.3.6 Recommendation

Based on the above parametric study configuration of a proposed solar water heater can be recommended for Toronto, Ontario. The proposed design recommendation will have an 8-hour exposure time to supply a five person household requiring 350L of hot water, from an inlet temperature of $12°C$ to an outlet temperature of $60°C$. The exposure time is chosen as a realistic average of usable day-light, while the water load is chosen to provide for the largest possible considered scenario. From parametric analysis, the most suitable PCM for use should be the 0500-Q93 BioPCM™ as it provides a 77% reduction in required heat exchanger area for an increase of mass less than 15% when compared to $Na_2SiO_35H_2O$; rendering it a more desirable material for domestic usage where spatial restrictions are a concern. Conductivity of heat exchange tube will be equal to that of the default condition, Aluminium, to match realistic material selection. To reduce required size of heat exchanger for feasibility of domestic usage, the tube inner radius will be 3.5mm with a thickness of 1mm to encourage internal convective heat transfers. Chosen heat transfer coefficients for outer and inner surfaces will be $2000W/m^2K$ and $250W/m^2K$, respectively. Though further increase of the convective coefficients will result in a reduction of heat exchange surface area, very large values are difficult to achieve in these systems and will not reflect actuality. Table 3.5 lists the yielded required sizing for solar collector and heat exchanger based on the aforementioned parameters for the month of September in Toronto, Ontario.

Table 3.5: Recommended surface area of solar collector and heat exchanger for yearly usage in Toronto, Ontario

Required Solar Collector Surface Area (m^2)	Required Heat Exchang Surface Area(m^2)
11.01	256.7

The proposed configuration will be tested for altering magnitudes of solar irradiation, based on month of the year, to determine the amount of domestic energy it can supply. The supplied solar energy per month, also known as "Solar Fraction", will dictate how efficient the Solar Collector's sizing will be for year round performance at a specific location. Total solar collector

area is to be divide into multiple dishes of desired diameter to improve practicality of domestic application. Results of solar fraction for Toronto, Ontario based on average monthly insolation for Canada is presented in Fig. 3.16.
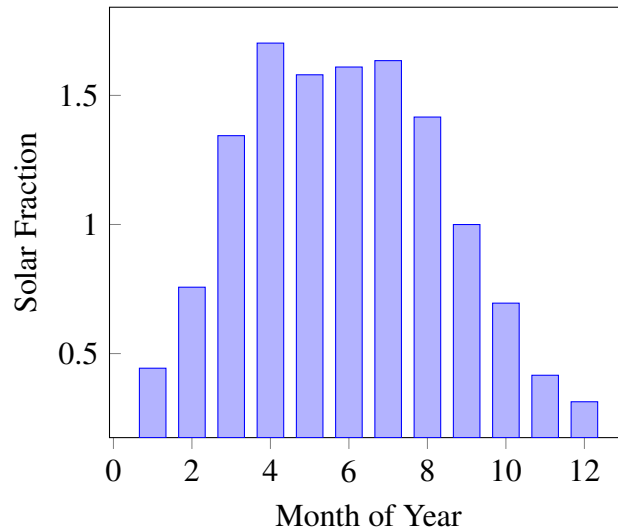
Figure 3.16: Solar fractions produced by proposed solar collector sizing

The solar fractions calculated depict the proposed system will be able to maintain a full supply of heated water for the months of March through September. Once the Winter months approach, the sizing of the dish is significantly inadequate for daily supply due to extremely low values of insolation. The low solar fractions for the above mentioned months indicate that a secondary, auxiliary heater be integrated to a domestic water heater to account for periods of low insolation. During the Summer, however, the solar fraction exceeds 1, rendering the sizing more than appropriate for that period of time. Reduction of size to account for the excess solar fraction produced in Summer will only further reduce the effectiveness of the solar collector during Winter; thus to fully optimize sizing of the Solar collector this seasonal trade off must be considered.

Chapter 4

Summary

The objective of this study was to develop a novel "Optical Guide" system for a more efficient transfer of radiative solar energy in parabolic dish solar collector systems compared to that of traditional methodologies. The optical guide and corresponding parabolic dish solar collector configuration were then integrated to a theoretical model with a latent thermal energy storage system to parametrically investigate its feasibility for domestic heating applications. Two ray trace software programs, Tracer^{TM} and SolTrace^{TM} were used to analyse the proposed catropic system which consisted of two parabolic dish collectors in a Gregorian-secondary configuration, a flat plate reflector and optical conduit for means of absorbing collected ray bundles in the thermal reservoir at the bottom surface.

SolTrace^{TM} generated more consistent results of average flux intensity over all altitude angles, along with producing illustrations of higher resolution for flux distribution. It is because of these benefits that SolTrace^{TM} provides a more reliable data set for the proposed objective than Tracer^{TM}. With the flat plate mirror angled $25°$ greater than the incident angle of the solar collector, areas of high intensity were depicted in the centre of the reservoir, indicating theoretical temperatures higher than the surrounding areas. High intensity locations can be detrimental to the solar collector system as the latent heat storage material or optical guide can deteriorate when subjected to high temperatures; thus suitable materials must be chosen to accommodate for this distribution, or, variation in orientation of collector components need to be made to alter local intensities. Absorbed radiative flux distribution will dictate the heating mechanisms in the phase change material, thus being able to reliably alter it will allow for desirable heat input to the selected material.

The set of default conditions tested for Toronto, Ontario during the month of September yielded a increase in required solar collector area for an increase in water load and a decrease in area for greater exposure times. When compared to Red Deer, Alberta, a location of higher insolation, these requirements for area decreased significantly. Phase change material for use in latent heat storage depicted larger mass requirements when latent heat of fusion is reduced for analogous conditions; but lower heat exchange area for higher melting temperatures regardless of latent heat. This trade off will be crucial in determining location of solar water heaters as variation of incident solar irradiation can be accommodated by phase change material selection. Parametric study of latent heat storage integration indicated a higher influence of convective heat transfer when compared to that of conductive mechanisms for surface area requirements of the heat exchanger. Increasing convection coefficients provide a significant reduction in heat exchanger

area up to a limit of approximately $h_o = 2000W/m^2K$ and $h_i = 250W/m^2K$ where further increases can be rendered negligible. Internal radius has a higher correlation to reduction of heat exchange area, thus internal heat transfers, across varying water loads than tube thickness as its influence on both internal convection coefficient and total thermal resistance is significantly greater than the tube thickness. Thermal conductivity of the material chosen for the tube has a negligible influence on heat exchanger area as an increase in thermal conductivity produces insignificant area reductions. Results indicate a suitable location and phase change material must be determined to optimize solar water heater sizing based on its operating conditions; with thin tubes encouraging the greatest rates of heat transfer.

To further improve the development of the proposed optical guide, research must continue. A scaled down model of the Gregorian-secondary configuration along with optical guide should be experimentally tested to indicate accuracy of results depicted in SolTrace^{TM}. It is suggested that a 3D printed model of the solar collectors be configured with a similarly created optical guide and covered in reflective coating to examine heat flux distribution and temperatures developed in the thermal reservoir. Heat transfer within the phase change material under a specifically defined flux distribution must be understood in order to produce the optimal location of solar collector components. Once behaviour of the phase change material is understood, the computational modelling techniques defined can be used to generate a distribution that will encourage heat transfer within the PCM and not damage its material integrity. Further study of phase change material must be conducted to experimentally define the outer heat transfer coefficient to generate the most accurate sizing requirements based on the theoretical water heater model. The introduction of baffles and various heat exchanger configurations must also be further investigated for assumptions in the current model to more closely match that of a realistic situation, as heat transfer mechanisms in charging and discharging of PCMs are not verbatim to sole phase change of condensation or vaporization as assumed. Future considerations include large scale production of the solar water heater, such as industrial usage or for usage in power plants as solar collector sizing requirements may not be appealing for domestic usage in areas of low insolation.

Bibliography

[1] Alessandro Clerici and G Alimonti. World energy resources. In *EPJ Web of Conferences*, volume 98, page 01001. EDP Sciences, 2015.

[2] US EIA. Primary energy consumption by source and sector, 2012, 2015.

[3] World oil statistics (edition 2016). *IEA Oil Information Statistics*, 2012.

[4] Frederica Perera. Pollution from fossil-fuel combustion is the leading environmental threat to global pediatric health and equity: solutions exist. *International journal of environmental research and public health*, 15(1):16, 2018.

[5] International Energy Agency. *CO2 Emissions from Fuel Combustion 2001*. 2001.

[6] U.s. energy information administration - eia - independent statistics and analysis.

[7] Natural Resources Canada Government of Canada. Energy Use in Canada: Trends Publications, September 2011.

[8] Carmen Aguilar and David L. Ryan. Domestic water heating and water heater energy consumption in canada. 2005.

[9] World Health Organization. *Air quality guidelines: global update 2005: particulate matter, ozone, nitrogen dioxide, and sulfur dioxide*. World Health Organization, 2006.

[10] David Hofmann, James Butler, Thomas Conway, Edward Dlugokencky, James Elkins, Kenneth Masarie, Stephen Montzka, Russell Schnell, and Pieter Tans. The noaa annual greenhouse gas index (aggi). 01 2011.

[11] China energy outlook. *World Energy Outlook 2017 World Energy Outlook*, 2017.

[12] Reza Karimi, Touraj Tavakoli Gheinani, and Vahid Madadi Avargani. A detailed mathematical model for thermal performance analysis of a cylindrical cavity receiver in a solar parabolic dish collector system. *Renewable Energy*, 125:768 – 782, 2018.

[13] T. Sokhansefat, A.b. Kasaeian, and F. Kowsary. Heat transfer enhancement in parabolic trough collector tube using al2o3/synthetic oil nanofluid. *Renewable and Sustainable Energy Reviews*, 33:636–644, 2014.

[14] Alibakhsh Kasaeian, Samaneh Daviran, Reza Danesh Azarian, and Alimorad Rashidi. Performance evaluation and nanofluid using capability study of a solar parabolic trough collector. *Energy Conversion and Management*, 89:368–375, 2015.

[15] Unknown. Solar colelctors. `http://encyclopedia.che.engin.umich.edu/Pages/EnergyTransfer/SolarThermal/SolarThermalEnergyGeneration.html`.

[16] Ziyad Salameh. Chapter 5 - emerging renewable energy sources. In Ziyad Salameh, editor, *Renewable Energy System Design*, pages 299 – 371. Academic Press, Boston, 2014.

[17] Ramola Sinha and Nitin P. Gulhane. Numerical study of radiation heat loss from solar cavity receiver of parabolic dish collector. *Numerical Heat Transfer, Part A: Applications*, 77(7):743–759, 2020.

[18] Natthaphon Roonprasang, Pichai Namprakai, and Naris Pratinthong. A solar water heater system self circulated by a steam power. 08 2020.

[19] N.M Nahar. Capital cost and economic viability of thermosyphonic solar water heaters manufactured from alternate materials in india. *Renewable Energy*, 26(4):623 – 635, 2002.

[20] Zhangyuan Wang, Zicong Huang, Siming Zheng, and Xudong Zhao. 6 - solar water heaters. In Trevor M. Letcher and Vasilis M. Fthenakis, editors, *A Comprehensive Guide to Solar Energy Systems*, pages 111 – 125. Academic Press, 2018.

[21] Zhangyuan Wang, Peng Guo, Haijing Zhang, Wansheng Yang, and Sheng Mei. Comprehensive review on the development of sahp for domestic hot water. *Renewable and Sustainable Energy Reviews*, 72:871 – 881, 2017.

[22] Ioan Sarbu and Calin Sebarchievici. Chapter 4 - thermal energy storage. In Ioan Sarbu and Calin Sebarchievici, editors, *Solar Heating and Cooling Systems*, pages 99 – 138. Academic Press, 2017.

[23] Ibrahim Dincer. On thermal energy storage systems and applications in buildings. *Energy and Buildings*, 34(4):377 – 388, 2002.

[24] B Kelly and D Kearney. Thermal storage commercial plant design study for a 2-tank indirect molten salt system: Final report, 13 may 2002 - 31 december 2004.

[25] C.W. Chan, J. Ling-Chin, and A.P. Roskilly. Reprint of "a review of chemical heat pumps, thermodynamic cycles and thermal energy storage technologies for low grade heat utilisation". *Applied Thermal Engineering*, 53(2):160 – 176, 2013. Includes Special Issue: PRO-TEM Special Issue.

[26] M. Medrano, M.O. Yilmaz, M. Nogués, I. Martorell, Joan Roca, and Luisa F. Cabeza. Experimental evaluation of commercial heat exchangers for use as pcm thermal storage systems. *Applied Energy*, 86(10):2047 – 2055, 2009.

[27] Vincent Basecq, Ghislain Michaux, Christian Inard, and Patrice Blondeau. Short-term storage systems of thermal energy for buildings: a review. *Advances in Building Energy Research*, 7(1):66–119, 2013.

[28] Benoît Stutz, Nolwenn Le Pierres, Frédéric Kuznik, Kevyn Johannes, Elena Palomo Del Barrio, Jean-Pierre Bédécarrats, Stéphane Gibout, Philippe Marty, Laurent Zalewski, Jerome Soto, Nathalie Mazet, Régis Olives, Jean-Jacques Bezian, and Doan Pham Minh. Storage of thermal solar energy. *Comptes Rendus Physique*, 18(7):401 – 414, 2017. Demain l'énergie.

[29] Steven Jevnikar and Kamran Siddiqui. Investigation of the influence of heat source orientation on the transient flow behavior during pcm melting using particle image velocimetry. *Journal of Energy Storage*, 25:100825, 2019.

[30] M.H. Mahfuz, M.R. Anisur, M.A. Kibria, R. Saidur, and I.H.S.C. Metselaar. Performance investigation of thermal energy storage system with phase change material (pcm) for solar water heating application. *International Communications in Heat and Mass Transfer*, 57:132 – 139, 2014.

[31] A. Abhat. Low temperature latent heat thermal energy storage: Heat storage materials. *Solar Energy*, 30(4):313 – 332, 1983.

[32] Mohammad Bashar and Kamran Siddiqui. Experimental investigation of transient melting and heat transfer behavior of nanoparticle-enriched pcm in a rectangular enclosure. *Journal of Energy Storage*, 18:485 – 497, 2018.

[33] S.C. Bhatia. 2 - solar radiations. In S.C. Bhatia, editor, *Advanced Renewable Energy Systems*, pages 32 – 67. Woodhead Publishing India, 2014.

[34] Michael E. Loik, Sue A. Carter, Glenn Alers, Catherine E. Wade, David Shugar, Carley Corrado, Devin Jokerst, and Carol Kitayama. Wavelength-selective solar photovoltaic systems: Powering greenhouses for plant growth at the food-energy-water nexus. *Earth's Future*, 5(10):1044–1053, 2017.

[35] Zoltan Szantoi. *Electromagnetic Spectrum*. 10 2013.

[36] Claus Fröhlich. *Solar Constantsolar constantand Total Solar Irradiance Variationstotal solar irradiance (TSI)variations*, pages 399–416. Springer New York, New York, NY, 2013.

[37] Damien Buie and A. Monger. The effect of circumsolar radiation on a solar concentrating system. *Solar Energy - SOLAR ENERG*, 76:181–185, 03 2004.

[38] Ye Wang, Daniel Potter, Charles-Alexis Asselineau, Clotilde Corsi, Michael Wagner, Cyril Caliot, Benjamin Piaud, Manuel Blanco, Jin-Soo Kim, and John Pye. Verification of optical modelling of sunshape and surface slope error for concentrating solar power systems. *Solar Energy*, 195:461 – 474, 2020.

[39] J Kleinwaechter, H Kleinwaechter, and W Beale. Recent advances in design of low cost film concentrator and low pressure free piston stirling engines for solar power. 1984.

[40] PL Panda, Toshio Fujita, and JW Lucas. Summary assessment of solar thermal parabolic dish technology for electrical power generation. Technical report, Jet Propulsion Lab., Pasadena, CA (USA), 1985.

[41] R Zheng, Rich Diver, D Caldwell, B Fritz, R Cameron, P Humble, W TeGrotenhuis, R Dagle, and R Wegeng. Integrated solar thermochemical reaction system for steam methane reforming. *Energy Procedia*, 69:1192–1200, 2015.

[42] Keith Lovegrove, Andreas Luzzi, I Soldiani, and Holger Kreetz. Developing ammonia based thermochemical energy storage for dish power plants. *Solar energy*, 76(1-3):331–337, 2004.

[43] Daniel J Alpert, Thomas R Mancini, Richard M Houser, James W Grossman, Paul Schissel, Meir Carasso, Gary Jorgensen, and Martin Scheve. Solar concentrator development in the united states. *Solar energy materials*, 24(1-4):307–319, 1991.

[44] Umer Jamil and Wajahat Ali. Performance tests and efficiency analysis of solar invictus 53s–a parabolic dish solar collector for direct steam generation. In *AIP Conference Proceedings*, volume 1734, page 070018. AIP Publishing LLC, 2016.

[45] Umberto Desideri and Pietro Elia Campana. Analysis and comparison between a concentrating solar and a photovoltaic power plant. *Applied Energy*, 113:422 – 433, 2014.

[46] Khem Raj Gautam and Gorm Bruun Andresen. Performance comparison of building-integrated combined photovoltaic thermal solar collectors (bipvt) with other building-integrated solar technologies. *Solar Energy*, 155:93 – 102, 2017.

[47] Mona M Naim and Mervat A Abd El Kawi. Non-conventional solar stills part 2. non-conventional solar stills with energy storage element. *Desalination*, 153(1-3):71–80, 2003.

[48] Abdulhaiy M Radhwan. Transient performance of a stepped solar still withbuilt-in latent heat thermal energy storage. *Desalination*, 171(1):61–76, 2005.

[49] Eman-Bellah S. Mettawee and Ghazy M.R. Assassa. Experimental study of a compact pcm solar collector. *Energy*, 31(14):2958 – 2968, 2006.

[50] Hussain H. Al-Kayiem and Saw C. Lin. Performance evaluation of a solar water heater integrated with a pcm nanocomposite tes at various inclinations. *Solar Energy*, 109:82 – 92, 2014.

[51] Monia Chaabane, Hatem Mhiri, and Philippe Bournot. Thermal performance of an integrated collector storage solar water heater (icsswh) with phase change materials (pcm). *Energy Conversion and Management*, 78:897 – 903, 2014.

[52] Suat Canbazoğlu, Abdulmuttalip Şahinaslan, Ahmet Ekmekyapar, Ý. Gökhan Aksoy, and Fatih Akarsu. Enhancement of solar thermal energy storage performance using sodium thiosulfate pentahydrate of a conventional solar water-heating system. *Energy and Buildings*, 37(3):235 – 242, 2005.

[53] K. Chuawittayawuth and S. Kumar. Experimental investigation of temperature and flow distribution in a thermosyphon solar water heating system. *Renewable Energy*, 26(3):431 – 448, 2002.

[54] Natthaphon Roonprasang, Pichai Namprakai, and Naris Pratinthong. Experimental studies of a new solar water heater system using a solar water pump. *Energy*, 33(4):639 – 646, 2008.

[55] Abdul-Jabbar N. Khalifa. Forced versus natural circulation solar water heaters: A comparative performance study. *Renewable Energy*, 14(1):77 – 82, 1998. 6th Arab International Solar Energy Conference: Bringing Solar Energy into the Daylight.

[56] Dong Won Lee and Atul Sharma. Thermal performances of the active and passive water heating systems based on annual operation. *Solar Energy*, 81(2):207 – 215, 2007.

[57] N.M. Nahar and K.S. Malhotra. Year round performance of a cylindrical solar water heater. *Energy Conversion and Management*, 24(4):277 – 280, 1984.

[58] James Zucchetto and Sandra Brown. Comparison of the fossil fuel energy requirements for solar, natural gas, and electrical water heating systems. *Resource Recovery and Conservation*, 2(4):283 – 300, 1977.

[59] Charles G. Rupert. Mathematics of the reflecting telescope. *Popular Astronomy*, 26:525, January 1918.

[60] R.N. Wilson. *Reflecting Telescope Optics I: Basic Design Theory and its Historical Development*. Astronomy and Astrophysics Library. Springer Berlin Heidelberg, 2007.

[61] John A. Duffie, William A. Beckman, and John A. Duffie. *Solar energy thermal processes, chapters 1-7*. Engineering Experiment Station, University of Wisconsin–Madison, 1978.

[62] L.d. Jaffe and P.t. Poon. Secondary and compound concentrators for parabolic-dish solar-thermal power systems. 1981.

[63] Vladimir Sacek. Telescope optics. `https://www.telescope-optics.net/two-mirror.htm`.

[64] J. Robert Mahan. Fundamentals of Ray Tracing. In *The Monte Carlo Ray-Trace Method in Radiation Heat Transfer and Applied Optics*. ASME Press, 02 2019.

[65] George B. Rybicki and Alan P. Lightman. *Radiative processes in astrophysics*. Wiley-VCH Verlag, 2004.

[66] Physical constants: 2010 codata recommended values. *Field Guide to Radiometry*, page 90–90.

[67] Robert Siegel and John R. Howell. *Thermal radiation heat transfer*. Scientific and Technical Information Division, National Aeronautics and Space Administration, 1968.

[68] Frank P. Incropera and David P. DeWitt. *Fundamentals of heat transfer*. Wiley, 1981.

[69] Robert Siegel. Thermal radiation heat transfer, fourth edition, Dec 2001.

[70] J. Robert Mahan. Fundamentals of Thermal Radiation. In *The Monte Carlo Ray-Trace Method in Radiation Heat Transfer and Applied Optics*. ASME Press, 02 2019.

[71] Christian P. Robert and George Casella. *Monte Carlo statistical methods*. Springer, 2010.

[72] J. R. Mahan. *The Monte Carlo ray-trace method in radiation heat transfer and applied optics*. The American Society of Mechanical Engineers, 2019.

[73] Anders Ångström. *The solar constant and the temperature of the earth*, volume 3. 1965.

[74] Tim Wendelin, Aron Dobos, and Allan Lewandowski. Soltrace: A ray-tracing code for complex solar optical systems. Jan 2013.

[75] Tim Wendelin. Soltrace: A new optical modeling tool for concentrating solar optics. *Solar Energy*, Jan 2003.

[76] Anant Shukla, D. Buddhi, and R.L. Sawhney. Solar water heaters with phase change material thermal energy storage medium: A review. *Renewable and Sustainable Energy Reviews*, 13(8):2119 – 2125, 2009.

[77] B. Fortunato, S.M. Camporeale, M. Torresi, and M. Albano. Simple mathematical model of a thermal storage with pcm. *AASRI Procedia*, 2:241 – 248, 2012. AASRI Conference on Power and Energy Systems.

[78] Sebastian Kuboth, Andreas König-Haagen, and Dieter Brüggemann. Numerical analysis of shell-and-tube type latent thermal energy storage performance with different arrangements of circular fins. *Energies*, 10:274, 02 2017.

[79] Yuqiang Li, Gang Liu, Xianping Liu, and Shengming Liao. Thermodynamic multi-objective optimization of a solar-dish brayton system based on maximum power output, thermal efficiency and ecological performance. *Renewable Energy*, 95:465 – 473, 2016.

[80] Solargis. Solar global irradiance.

[81] Annabelle Joulin, Zohir Younsi, Laurent Zalewski, Stéphane Lassue, Daniel R. Rousse, and Jean-Paul Cavrot. Experimental and numerical investigation of a phase change material: Thermal-energy storage and release. *Applied Energy*, 88(7):2454 – 2462, 2011.

[82] Ruijun Pan. Energy density and volume expansion in solid-liquid phase change, for energy applications, 2013.

[83] T.L. Bergman, F.P. Incropera, D.P. DeWitt, and A.S. Lavine. *Fundamentals of Heat and Mass Transfer*. Wiley, 2011.

[84] HA Navarro and LC Cabezas-Gomez. Effectiveness-ntu computation with a mathematical model for cross-flow heat exchangers. *Brazilian Journal of Chemical Engineering*, 24(4):509–521, 2007.

[85] Danny S Parker and Philip W Fairey. Estimating daily domestic hot-water use in north american homes. 2015.

[86] Environment Canada and Climate Change. Government of canada / gouvernement du canada, Dec 2019.

[87] Alain Moreau and François Laurencelle. Field study of solar domestic water heaters in quebec. *Energy Procedia*, 30:1331–1338, 12 2012.

[88] Hassan Nazir, Mariah Batool, Francisco J. Bolivar Osorio, Marllory Isaza-Ruiz, Xinhai Xu, K. Vignarooban, Patrick Phelan, Inamuddin, and Arunachala M. Kannan. Recent developments in phase change materials for energy storage applications: A review. *International Journal of Heat and Mass Transfer*, 129:491 – 523, 2019.

[89] Albert Castell, Cristian Solé, Marc Medrano, Joan Roca, Luisa F. Cabeza, and Daniel García. Natural convection heat transfer coefficients in phase change material (pcm) modules with external vertical fins. *Applied Thermal Engineering*, 28(13):1676 – 1686, 2008.

[90] Phase change energy solutions: Leader in efficient building materials, Mar 2018.

[91] Solartron. Solar dish specifications. `https://www.solartronenergy.com/solar-concentrator/specifications/`.
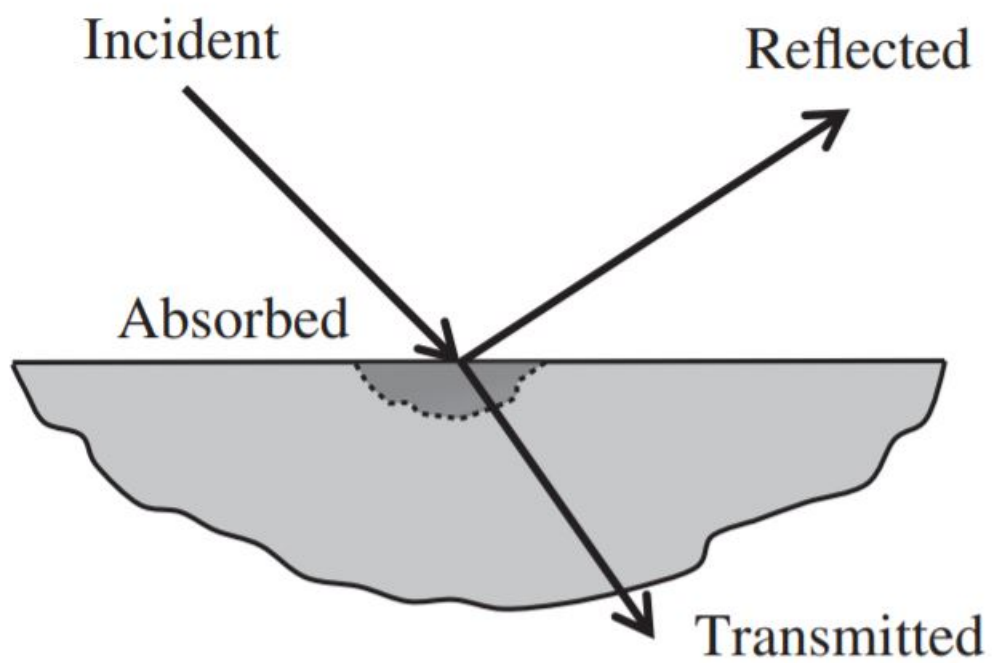
Appendices

Appendix A

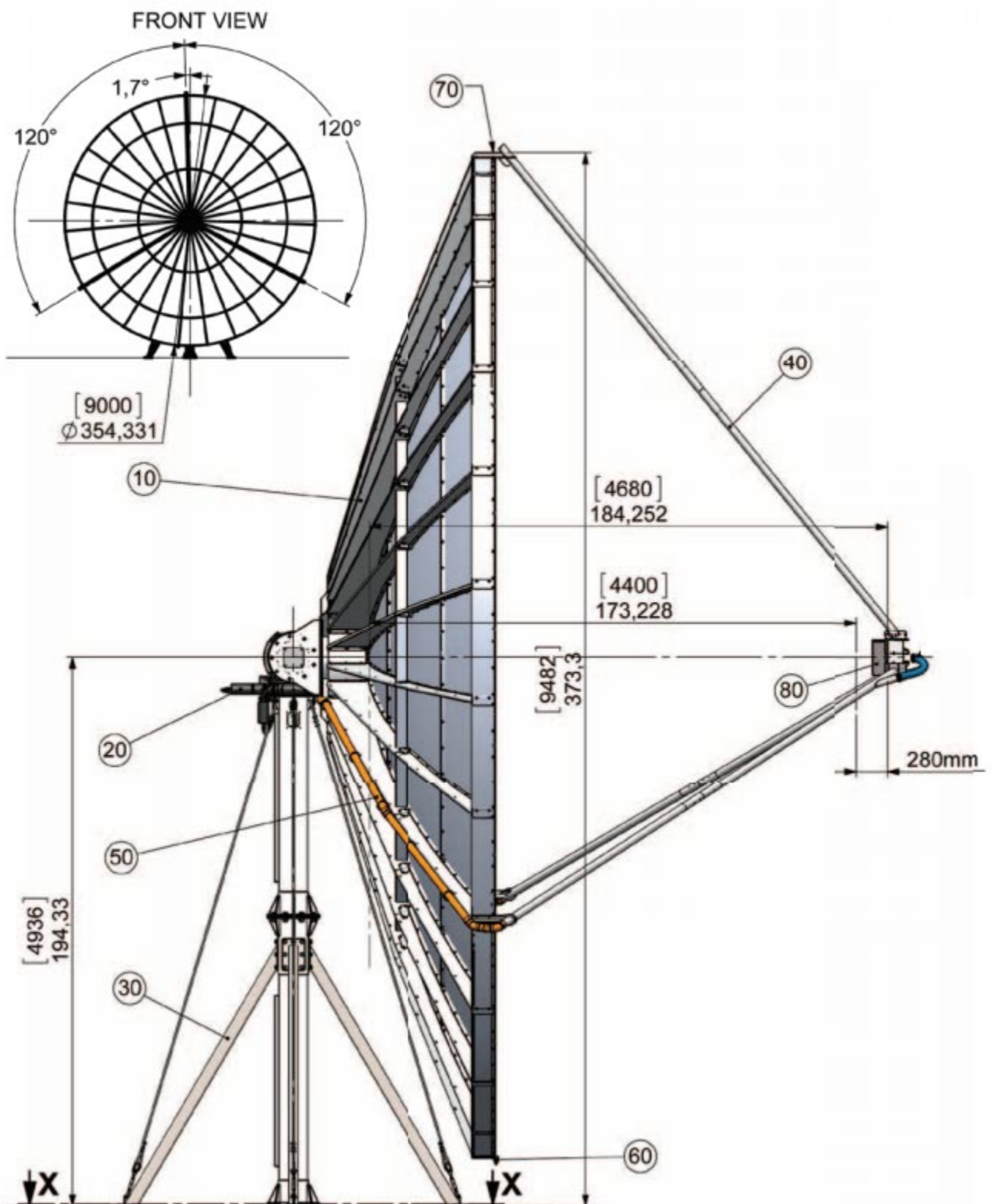Figure A1: Dispersion of Incident Radiance on a Surface [70]

Appendix B

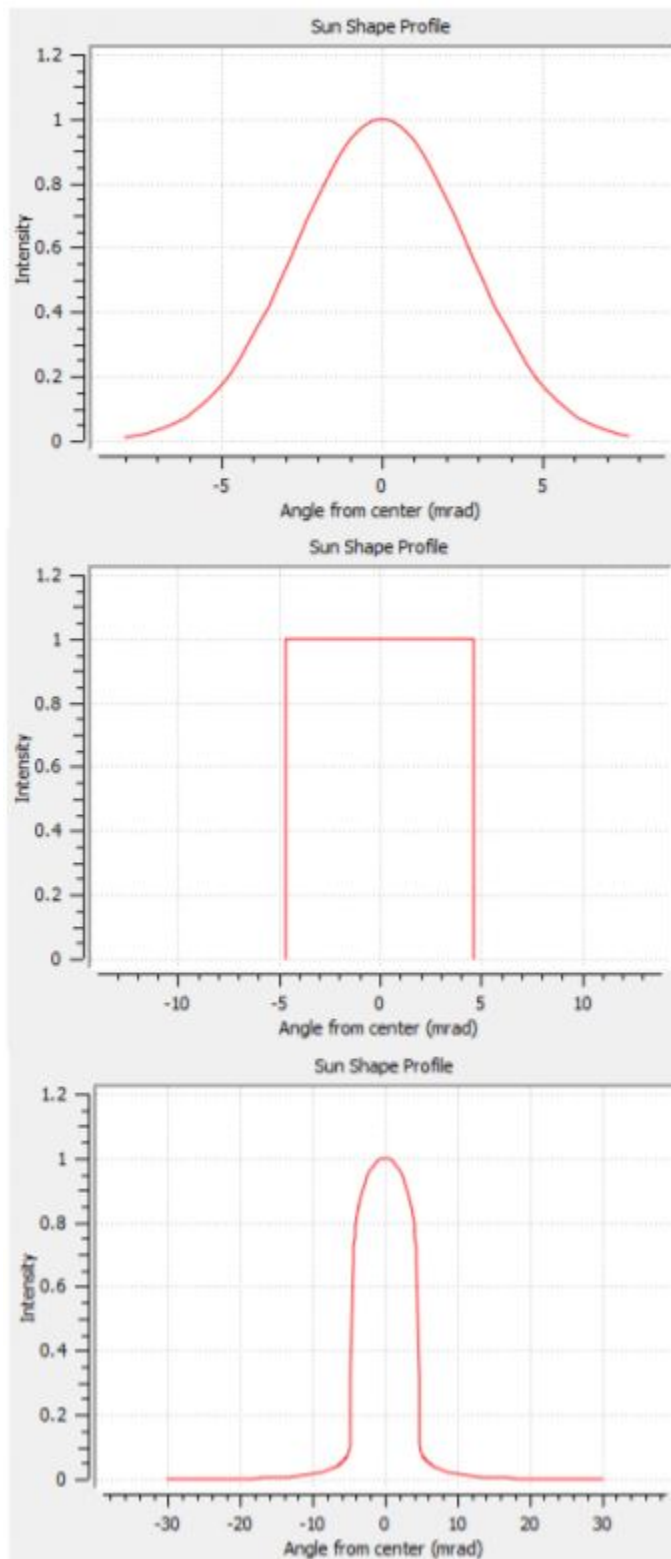Figure B1: Solartron Solar Dish Collector [91]

Appendix C

Figure C1: Sun Shapes: Gaussian, Pillbox and User Defined Datum
[74]

74

Appendix D

$$Q_w = m_w C_{p,w}(T_{o,w} - T_{i,w})$$

$$Q_w = 70 * 997 * 4.1 * (60 - 12)$$

$$Q_w = 13734.67[kJ]$$

$$Q_{pcm} = Q_w = m_{pcm}(C_{p,s}\Delta T_s + L_f + C_{p,l}\Delta T_l)$$

$$m_{pcm} = \frac{Q_{pcm}}{(C_{p,s}\Delta T_s + L_f + C_{p,l}\Delta T_l)}$$

$$m_{pcm} = \frac{13734}{(2.3 * (72.2 - 57.2)) + 267 + (4.57 * (87.2 - 72.2))}$$

$$m_{pcm} = 45.09[kg]$$

$$V_{pcm} = \frac{m_{pcm}}{\rho_{pcm,l}}$$

$$V_{pcm} = \frac{45.09}{1280}$$

$$V_{pcm} = 0.035233103[m^3]$$

$$Q_{sc} = \dot{Q}_w = \frac{Q_w}{t} = \eta_{sc}I_{sc}A_{sc}$$

$$Q_{sc} = \frac{13734[kJ]}{6[h] * 3600[\frac{s}{h}]}$$

$$Q_{sc} = 0.6358[kW] = 635.8[W]$$

$$A_{sc} = \frac{Q_{sc}}{I_{sc}\eta_{sc}}$$

$$A_{sc} = \frac{635}{228.71 * 0.75} = 2.936[m^2]$$

Figure D1: Sample Calculation for Solar Collector Area and PCM Volume and Mass Under
Default Operating Conditions for 70L Water Load and 6h Exposure Time

Appendix E

$$Nu = \frac{h_i D_h}{k} = 3.66$$

$$h_i = \frac{3.66 k_w}{D_h} = \frac{3.66k}{2r_i}$$

$$h_i = \frac{3.66 * 0.613}{2 * 0.006} = 186.95 [W/m^2 K]$$

$$\dot{m}_w = \frac{Q_w}{C_{p,w}(T_{o,w} - T_{i,w})t}$$

$$\dot{m}_w = \frac{635.8}{4.178 * (60 - 12)}$$

$$\dot{m}_w = 3.23 [kg/s]$$

$$\Delta T_o = T_m - To, w = 72.2 - 60 = 12.2 [^\circ C]$$

$$\Delta T_i = T_m - Ti, w = 72.2 - 12 = 60.2 [^\circ C]$$

$$R_{tot} = -\frac{1}{\dot{m}_w C_{p,w} ln(\frac{\Delta T_o}{\Delta T_i})}$$

$$R_{tot} = -\frac{1}{3.23 * 4.178 * ln(12.2/60.2)}$$

$$R_{tot} = 4.64 \cdot 10^{-5} [K/m]$$

$$\frac{1}{U} = \frac{r_o}{r_i h_i} + \frac{r_o}{k} ln(\frac{r_o}{r_i}) + \frac{1}{h_o}$$

$$\frac{1}{U} = \frac{0.008}{0.006 * 186.95} + \frac{0.008}{205} ln(\frac{0.008}{0.006}) + \frac{1}{1800}$$

$$\frac{1}{U} = 0.0059 [m^2 K/W]$$

$$U = 169.48 [W/m^2 K]$$

$$A_{hx} = \frac{1}{U R_{tot}}$$

$$A_{hx} = \frac{1}{169.48 * 4.64 \cdot 10^{-5}}$$

$$A_{hx} = 127.135 [m^2]$$

Figure E1: Sample Calculation for Heat Exchanger Area Under Default Operating Conditions
for 70L Water Load and 6h Exposure Time

Curriculum Vitae

Name: Zane Charran

Post-Secondary University of Western Ontario
Education and London, Ontario
Degrees: 2014 - 2018 BESc.

Related Work Teaching Assistant
Experience: The University of Western Ontario
2018 - 2020